

## LEPTON ACCELERATION IN THE VICINITY OF THE EVENT HORIZON: HIGH-ENERGY AND VERY-HIGH-ENERGY EMISSIONS FROM ROTATING BLACK HOLES WITH VARIOUS MASSES

KOUICHI HIROTANI<sup>1</sup>, HUNG-YI PU<sup>1</sup>, LUPIN CHUN-CHE LIN<sup>1</sup>, HSIANG-KUANG CHANG<sup>2</sup> MAKOTO INOUE<sup>1</sup>, ALBERT K. H KONG<sup>2</sup>, SATOKI MATSUSHITA<sup>1</sup>, AND PAK-HIN T. TAM<sup>3</sup><sup>1</sup> Academia Sinica, Institute of Astronomy and Astrophysics (ASIAA), PO Box 23-141, Taipei, Taiwan 10617, R.O.C.;  
hirotani@tiara.sinica.edu.tw<sup>2</sup> Institute of Astronomy, Department of Physics, National Tsing Hua University, No. 101, Section 2, Kuang-Fu Road, Hsinchu, Taiwan 30013, R.O.C. and<sup>3</sup> School of Physics and Astronomy, Sun Yat-Sen University, Zhuhai 519082, China

## ABSTRACT

We investigate the electrostatic acceleration of electrons and positrons in the vicinity of the event horizon, applying the pulsar outer-gap model to black hole magnetospheres. During a low accretion phase, the radiatively inefficient accretion flow (RIAF) cannot emit enough MeV photons that are needed to sustain the force-free magnetosphere via two-photon collisions. In such a charge-starved region (or a gap), an electric field arises along the magnetic field lines to accelerate electrons and positrons into ultra-relativistic energies. These relativistic leptons emit copious gamma-rays via curvature and inverse-Compton (IC) processes. Some of such gamma-rays collide with the submillimeter-IR photons emitted from the RIAF to materialize as pairs, which polarize to partially screen the original acceleration electric field. It is found that the gap gamma-ray luminosity increases with decreasing accretion rate. However, if the accretion rate decreases too much, the diminished RIAF soft photon field can no longer sustain a stationary pair production within the gap. As long as a stationary gap is formed, the magnetosphere becomes force-free outside the gap by the cascaded pairs, irrespective of the BH mass. If a nearby stellar-mass black hole (BH) is in quiescence, or if a galactic intermediate-mass BH is in a very low accretion state, its curvature and IC emissions are found to be detectable with *Fermi*/LAT and imaging atmospheric Cherenkov telescopes (IACT). If a low-luminosity active galactic nucleus is located within a few tens of Mpc, the IC emission from its super-massive BH is marginally detectable with IACT.

*Subject headings:* acceleration of particles — stars: black holes — gamma rays: stars — magnetic fields — methods: analytical — methods: numerical

## 1. INTRODUCTION

It is widely accepted that an accreting black hole (BH) of an arbitrary size can produce a pair of relativistic plasma jets, which are often observed in various wavelengths from radio to very-high-energy (VHE)  $\gamma$ -rays. The most plausible mechanism for powering such jets is the extraction of the BH rotational energy through the Blandford-Znajek (BZ) process (Blandford & Znajek 1976). In this electromagnetic process, the magnetic field lines threading the event horizon exert a counter torque on it to spin down the BH, launching Poynting-flux-dominated outflows (Koide et al. 2002). Indeed, general relativistic (GR) magnetohydrodynamic (MHD) models show the existence of nearly steady, collimated, magnetically dominated jets in the polar regions (McKinney & Gammie 2004; Hirose et al. 2004), whose structures are similar to those in the force-free models (Hawley & Krolik 2006; McKinney & Narayan 2007a,b). Since the centrifugal-force barrier prevents plasma accretion towards the rotation axis, the magnetic energy density dominates the plasmas' rest-mass energy density in these polar funnels.

Even if the axial funnels are almost force-free in this sense, it is the electric current that sustains the electromagnetic power, and it is the charged particles that carry the electric current. That is, even under the assumption of masslessness, it must be the real charged particles that constitute the electric currents. In the direct vicinity of

the horizon, causality requires that positive (or negative) charges must flow into the horizon when an electric current flows into (or out from) the horizon. Since accreting plasmas cannot easily penetrate into the funnels, and since they cannot emit sufficient MeV photons that are capable of materializing as electron-positron pairs when the accretion rate is very low, we need a process of plasma supply deep within the magnetosphere somewhere above the horizon.

To contrive a plasma source in the vicinity of the horizon, Beskin et al. (1992) extended the pulsar outer-magnetospheric lepton accelerator model (Cheng et al. 1986a,b) to BH magnetospheres, and proposed the BH gap model. Extending this pioneering work, Hirotani & Okamoto (1998) demonstrated that a sufficient electric current can be supplied via copious pair production around super-massive BHs (SMBHs). However, the predicted  $\gamma$ -ray luminosity was too small to be detected by any instruments, because they assumed a substantial accretion rate (as in quasars), which leads to a very thin gap width along the magnetic field lines.

On these grounds, Neronov & Aharonian (2007) and Levinson & Rieger (2011) revisited the BH gap model and applied it the central BH of radio galaxy M87 (i.e., M87\*) and Srg A\*, adopting a much thicker gap width as large as the horizon radius. Their assumption of a thick gap was, indeed, reasonable, because such a low luminosity active galactic nucleus generally possesses a less

dense radiation field in the center and hence a geometrically extended gap slightly above the horizon. Then Broderick & Tchekhovskoy (2015) demonstrated that the two-stream instability does not grow in the ultra-relativistic, counter-streaming pairs in BH gaps. Subsequently, Hirotani & Pu (2016, hereafter HP16) showed that a gap arises around the so-called ‘null-charge surface’, on which the GR Goldreich-Julian (GJ) charge density vanishes, by solving the set of an inhomogeneous part of the Maxwell equations, lepton equations of motion, and the radiative transfer equation. Then they applied their BH-gap model to the radio galaxy IC310, whose central BH (i.e., IC310\*) is accreting plasmas at much smaller rate than the Eddington rate. They demonstrated that the gap width becomes as large as the horizon radius when the accretion rate is very low, and that the observed VHE flux during the flare cannot be reproduced by their BH gap model, unless the magnetic field becomes much stronger than the equipartition value with the plasma accretions. Noting that GR effects most importantly appear in the formation of the null-charge surface through frame dragging, they evaluated the GJ charge density general relativistically. However, they neglected the GR effects in any other terms of the basic equations as the first step, because the electromagnetic interaction dominates the gravitational one except for the direct vicinity of the horizon, and because the photons emitted from the horizon vicinity will not strongly affect the emission spectra due to redshift.

In the present paper, to further quantify the gap model, we include the GR effects in all the basic equations and calculations, extending the method of HP16. In the next section, we examine the detectability of BH gap emissions for various BH masses. Then in § 3, we describe the background space time and derive the GR GJ charge density in a rotating BH magnetosphere. We then formulate the basic equations of gap electrodynamics in § 4, and investigate their emission properties in § 5. In the final section, we discuss how to discriminate the gap emission from the jet emission.

## 2. DETECTABILITY OF GAP EMISSIONS

Since the gap liberate only a portion of the electromagnetic power extracted from a rotating BH, the upper limit of its luminosity can be given by the Blandford-Znajek power (Blandford & Znajek 1976)

$$L_{\text{BZ}} \approx 10^{21} a_*^2 M_1^2 B^2 \text{erg s}^{-1}, \quad (1)$$

where  $a_* \equiv a/r_g$  denotes the dimensionless BH’s spin parameter,  $a \equiv J/(Mc)$  the spin parameter,  $J$  the BH’s angular momentum,  $M$  the BH mass,  $c$  the speed of light,  $r_g \equiv GM/c^2$  the gravitational radius,  $G$  the gravitational constant,  $B$  the magnetic field strength in gauss, and  $M_1 \equiv M/(10M_\odot)$ .

In the present paper, unless explicitly mentioned, we assume that the magnetic buoyancy balances disk gravity and evaluate  $B$  with the equipartition value. Near the horizon, we obtain (Bisnovatyi-Kogan & Ruzmaikin 1974; Gosh et al. 1977; Narayan et al. 2003; Levinson & Rieger 2011)

$$B_{\text{eq}} \approx 4 \times 10^8 \dot{m}^{1/2} M_1^{-1/2} \text{G}, \quad (2)$$

where  $\dot{m}$  refers to the dimensionless accretion rate near

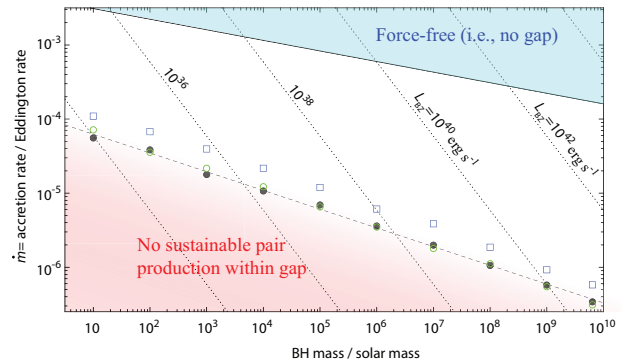


FIG. 1.— Dimensionless accretion rate,  $\dot{m}$ , versus black hole mass,  $M$ . The thick solid line shows the upper limit of  $\dot{m}$  above which the copious pair production by the RIAF emission prevents the formation of a gap (and ensures the force-free magnetosphere). The filled circles, open circles, and open squares denote the solved lower limits of  $\dot{m}$  (§ 5.4) for  $(a_*, \Omega_F/\omega_H, R_{\min}/r_g) = (0.9, 0.5, 6)$ ,  $(0.5, 0.5, 6)$ , and  $(0.9, 0.5, 12)$ , respectively. The thin dashed line shows a linear fit of the filled circles,  $\lg \dot{m}_{\text{low}} = -3.64 - 0.261 \lg(M/M_\odot)$ . The dotted lines show the extracted power from the black hole (eq. 1) for an extremely rotating case,  $a = M$ . For the explanation of the red-graded region, see the end of § 5.3.

the horizon and is defined as  $\dot{m} \equiv \dot{M}/\dot{M}_{\text{Edd}}$ ;  $\dot{M}$  denotes the mass accretion rate,  $\dot{M}_{\text{Edd}} \equiv L_{\text{Edd}}/\eta c^2$ ,  $L_{\text{Edd}} = 1.25 \times 10^{39} M_1 \text{ergs s}^{-1}$ , and  $\eta \approx 0.1$  (McKinney et al. 2012). Substituting  $B = B_{\text{eq}}$  into equation (1), we obtain

$$L_{\text{BZ}} \approx 1.7 \times 10^{38} a_*^2 \dot{m} M_1 \text{erg s}^{-1}. \quad (3)$$

The magnetosphere becomes force-free, that is, an electric field does not arise along the magnetic field lines, if the pair density exceeds the GJ value,  $N_{\text{GJ}} \sim \Omega_F B/(2\pi ce)$ , where  $\Omega_F$  denotes the angular frequency of the magnetic field and  $e$  the magnitude of the charge on the electron. In the vicinity of an accreting BH, a plasma accretion becomes radiatively inefficient when the accretion rate typically reduces to  $\dot{m} < 10^{-2.5}$  (Ichimaru 1977; Narayan & Yi 1994, 1995). From such a radiatively inefficient accretion flow (RIAF), MeV photons are emitted via free-free process, colliding each other to materialize as electron-positron pairs in the magnetosphere. If the number density,  $N_\pm$ , of such created pairs becomes less than  $N_{\text{GJ}}$ , charges cannot completely screen an electric field,  $E_\parallel$ , along the magnetic field line; that is, a gap (i.e., a charge-starved region) appears. The RIAF theory gives  $N_\pm$  as a function of  $M$  and  $\dot{m}$  (Levinson & Rieger 2011). Thus, putting  $N_\pm < N_{\text{GJ}}$ , we obtain a condition for a gap to appear,

$$\dot{m} < \dot{m}_{\text{up}} \equiv 3.1 \times 10^{-3} M_1^{-1/7}. \quad (4)$$

In figure 1, we plot this upper limit,  $\dot{m}_{\text{up}} = \dot{m}_{\text{up}}(M)$  as the thick solid line. The dotted lines denote  $L_{\text{BZ}}$  (eq. [3]) as labeled. The crossing of the solid line and a dotted line gives the Blandford-Znajek power at each BH mass. For example, the thick solid line and the dotted line labeled  $L_{\text{BZ}} = 10^{40} \text{ergs s}^{-1}$  cross at  $M \sim 10^6 M_\odot$ ; thus, we find that a super-massive BH with  $M \sim 10^6 M_\odot$  has a gap whose luminosity can attain up to  $10^{40} \text{ergs s}^{-1}$ .

To consider the case of an efficient energy extraction from a BH, we assume  $a_* = 0.9$  unless explicitly mentioned. Substituting  $\dot{m} = \dot{m}_{\text{up}}$  into equation (3), we then

obtain the maximum gap luminosity

$$L_{\text{BZ}} \approx 5.2 \times 10^{35} a_*^2 M_1^{6/7} \text{ ergs s}^{-1}. \quad (5)$$

Assuming that 100 % of this power is converted into radiation, we obtain the upper limit of its flux at Earth,  $F_{\text{BZ}} = L_{\text{BZ}}/4\pi d^2$ , where  $d$  is the distance to the BH.

For stellar-mass BHs, we obtain the flux upper limit,

$$F_{\text{BZ}} = \frac{L_{\text{BZ}}}{4\pi d^2} = 4.1 \times 10^{-9} a_*^2 M_1^{6/7} \left( \frac{d}{\text{kpc}} \right)^{-2} \text{ ergs s}^{-1} \text{ cm}^{-2}. \quad (6)$$

As will be seen in § 5.1, the gap emission spectrum peaks between GeV and 10 GeV for  $M \sim 10M_\odot$ . Thus, if a small portion of this BZ power (e.g., 0.1 %) is dissipated in the gap, we can expect a large time-averaged high-energy (HE) flux (e.g.,  $> 3 \times 10^{-12}$  ergs s $^{-1}$ ) that is detectable with *Fermi*/LAT. There is another component, which is formed by the inverse-Compton (IC) scatterings, appears in VHE. This component may be detectable with ground-based, imaging atmospheric Cherenkov telescopes (IACT). Note that equation (6) merely gives the upper limit, and that the actual photon flux can be obtained when we solve the gap electrodynamics from the basic equations. We will examine this issue in § 5.1.

For intermediate-mass BHs (IMBHs), we obtain the maximum flux of

$$F_{\text{BZ}} = 2.1 \times 10^{-9} a_*^2 M_3^{6/7} \left( \frac{d}{10 \text{ kpc}} \right)^{-2} \text{ ergs s}^{-1} \text{ cm}^{-2}, \quad (7)$$

where  $M_3 \equiv M/(10^3 M_\odot)$ . The spectrum has two peaks: the curvature photons peak in 1-10 GeV and the IC ones above TeV. Both spectral components are potentially detectable in HE and VHE, if an IMBH is located within our galaxy. We will examine this possibility in § 5.2.

For supermassive BHs, we obtain the maximum flux of

$$F_{\text{BZ}} = 3.0 \times 10^{-10} a_*^2 M_9^{6/7} \left( \frac{d}{10 \text{ Mpc}} \right)^{-2} \text{ ergs s}^{-1} \text{ cm}^{-2}, \quad (8)$$

where  $M_9 \equiv M/(10^9 M_\odot)$ . The IC component, which appears in VHE, may be detectable with IACT. We will examine this possibility in § 5.3.

### 3. BACKGROUND GEOMETRY AND THE NULL CHARGE SURFACE

The self-gravity of the plasma particles and the electromagnetic field little affects the space-time geometry. Thus, around a rotating BH, the background geometry is described by the Kerr metric (Kerr 1963). In the Boyer-Lindquist coordinates, it becomes (Boyer & Lindquist 1967)

$$ds^2 = g_{tt}dt^2 + 2g_{t\varphi}dtd\varphi + g_{\varphi\varphi}d\varphi^2 + g_{rr}dr^2 + g_{\theta\theta}d\theta^2, \quad (9)$$

where

$$g_{tt} \equiv -\frac{\Delta - a^2 \sin^2 \theta}{\Sigma} c^2, \quad g_{t\varphi} \equiv -\frac{2(GM/c^2)ar \sin^2 \theta}{\Sigma} c, \quad (10)$$

$$g_{\varphi\varphi} \equiv \frac{A \sin^2 \theta}{\Sigma}, \quad g_{rr} \equiv \frac{\Sigma}{\Delta}, \quad g_{\theta\theta} \equiv \Sigma; \quad (11)$$

$\Delta \equiv r^2 - 2(GM/c^2)r + a^2$ ,  $\Sigma \equiv r^2 + a^2 \cos^2 \theta$ ,  $A \equiv (r^2 + a^2)^2 - \Delta a^2 \sin^2 \theta$ . At the event horizon,  $\Delta$  vanishes,

giving  $r_{\text{H}} \equiv r_g + \sqrt{r_g^2 - a^2}$  as the horizon radius. If the BH is extremely rotating (i.e., if  $a \rightarrow r_g$ ) for instance, we obtain  $r_{\text{H}} \rightarrow r_g$ .

In a stationary and axisymmetric space time (as described by eq. 9), the Gauss's law becomes

$$\nabla_\mu F^{t\mu} = \frac{1}{\sqrt{-g}} \partial_\mu \left[ \frac{\sqrt{-g}}{\rho_w^2} g^{\mu\nu} (-g_{\varphi\varphi} F_{t\nu} + g_{t\varphi} F_{\varphi\nu}) \right] = \frac{4\pi}{c^2} \rho, \quad (12)$$

where  $\nabla$  denotes the covariant derivative, the Greek indices run over  $t, r, \theta, \varphi$ ;  $\sqrt{-g} = \sqrt{g_{rr}g_{\theta\theta}\rho_w^2} = c\Sigma \sin \theta$  and  $\rho_w^2 \equiv g_{t\varphi}^2 - g_{tt}g_{\varphi\varphi} = c^2 \Delta \sin^2 \theta$ ,  $\rho$  the real charge density. The electromagnetic fields are observed by an observer that is static with respect to asymptotic infinity, and are given by (Camenzind 1986a,b)  $E_r = F_{rt}$ ,  $E_\theta = F_{\theta t}$ ,  $E_\varphi = F_{\varphi t}$ ,  $B^r = (g_{tt} + g_{t\varphi}\Omega)F_{\theta\varphi}/\sqrt{-g}$ ,  $B^\theta = (g_{tt} + g_{t\varphi}\Omega)F_{\varphi r}/\sqrt{-g}$ ,  $B_\varphi = -\rho_w^2 F_{r\theta}/\sqrt{-g}$ , where  $F_{\mu\nu} \equiv \partial_\mu A_\nu - \partial_\nu A_\mu$  and  $A_\mu$  denotes the vector potential.

In this paper, we assume that the electromagnetic fields (i.e., all components of the Faraday tensor,  $F_{\mu\nu}$ ) depend on  $t$  and  $\varphi$  through  $\varphi - \Omega_F t$ . In this case, we can introduce the non-corotational potential  $\Phi$  such that

$$F_{\mu t} + \Omega_F F_{\mu\varphi} = -\partial_\mu \Phi(r, \theta, \varphi - \Omega_F t). \quad (13)$$

If  $F_{At} + \Omega_F F_{A\varphi} = 0$  holds for  $A = r$  and  $\theta$ ,  $\Omega_F \equiv F_{tr}/F_{r\varphi} = F_{t\theta}/F_{\theta\varphi}$  is conserved along the field line. However, in a particle acceleration region,  $F_{At} + \Omega_F F_{A\varphi}$  deviates from 0 and the magnetic field does not rigidly rotate. The deviation from rigid rotation is expressed in terms of  $\Phi$ , which gives the strength of the acceleration electric field measured by an observer that is static to asymptotic infinity as

$$E_{\parallel} \equiv \frac{\mathbf{B}}{B} \cdot \mathbf{E} = \frac{B^i}{B} (F_{it} + \Omega_F F_{i\varphi}) = \frac{\mathbf{B}}{B} \cdot (-\nabla \Phi), \quad (14)$$

where the Latin index  $i$  runs over spatial coordinates  $r, \theta, \varphi$ . Note that  $B^i F_{i\varphi} = 0$ .

Substituting Eq. (13) into (12), we obtain the Poisson equation for the non-corotational potential,

$$-\frac{c^2}{\sqrt{-g}} \partial_\mu \left( \frac{\sqrt{-g}}{\rho_w^2} g^{\mu\nu} g_{\varphi\varphi} \partial_\nu \Phi \right) = 4\pi(\rho - \rho_{\text{GJ}}), \quad (15)$$

where the GR Goldreich-Julian charge density is defined as

$$\rho_{\text{GJ}} \equiv \frac{c^2}{4\pi\sqrt{-g}} \partial_\mu \left[ \frac{\sqrt{-g}}{\rho_w^2} g^{\mu\nu} g_{\varphi\varphi} (\Omega_F - \omega) F_{\varphi\nu} \right]. \quad (16)$$

In the limit  $r \gg r_g$ , equation (16) reduces to the ordinary, special-relativistic expression (Goldreich & Julian 1969; Mestel 1971),

$$\rho_{\text{GJ}} \equiv -\frac{\mathbf{\Omega} \cdot \mathbf{B}}{2\pi c} + \frac{(\mathbf{\Omega} \times \mathbf{r}) \cdot (\nabla \times \mathbf{B})}{4\pi c}. \quad (17)$$

Therefore, the corrections due to magnetospheric currents, which are expressed by the second term of eq. (17), are included in equation (16).

In addition to  $F_{\mu\nu}$  and  $\Phi$ ,  $\rho$  may also depend on  $t$  and  $\varphi$  only through  $\varphi - \Omega_F t$ . In this case, equation (15) gives a 'stationary' gap solution in the 'co-rotational' frame, in the sense that  $\Phi$  and  $\rho$  are a function of  $r, \theta$ , and  $\varphi - \Omega_F t$ . Note that such stationary solutions are valid not only

between the two light surfaces (i.e., where  $k_0 \equiv -g_{tt} - 2g_{t\varphi}\Omega_F - g_{\varphi\varphi}\Omega_F^2 > 0$ ), but also inside the inner light surface and outside the outer light surface (i.e., where  $k_0 < 0$ ).

Equation (15) shows that  $E_{\parallel}$  is exerted along  $\mathbf{B}$  if  $\rho$  deviates from  $\rho_{\text{GJ}}$  in any region. In the close vicinity of the inner and outer boundaries, we can neglect the trans-field derivatives to obtain  $\partial_r E_{\parallel} \propto \rho - \rho_{\text{GJ}}$ . Thus,  $\partial_r E_{\parallel}$ , and hence  $\rho - \rho_{\text{GJ}}$  must have different signs at the two boundaries so that the gap may be closed. In a nearly vacuum gap,  $\rho \approx 0$  shows that  $\rho_{\text{GJ}}$  should change sign within the gap. Therefore, a gap should appear around the null-charge surface, where  $\rho_{\text{GJ}}$  vanishes. The null surface is, therefore, a natural place for a particle accelerator (i.e., a gap) to arise, in the same way as pulsar vacuum gap models (Holloway 1973; Chiang & Romani 1992; Romani 1996; Cheng et al. 2000).

It should be noted that the null surface appears **near** the place where  $\Omega_F$  coincides with the space-time dragging angular frequency,  $\omega$  (Beskin et al. 1992). The deviation of the null surface from this  $\omega(r, \theta) = \Omega_F$  surface is, indeed, small, as figure 1 of Hirotani & Okamoto (1998) indicates. Since  $\omega$  matches  $\Omega_F$  only near the horizon, the null surface, and hence the gap generally appears within one or two gravitational radii above the horizon, irrespective of the BH mass.

#### 4. MAGNETOSPHERIC LEPTON ACCELERATOR NEAR THE HORIZON

In this section, we formulate the BH-gap electrodynamics, extending the method described in Hirotani (2013) and HP16. Throughout this paper, we assume an aligned rotator in the sense that the magnetic axis coincides with the rotational axis of the BH, and seek an axisymmetric solution.

##### 4.1. Magnetic field structure

As described in HP16, a stationary BH gap is formed around the null surface, as long as the injected current density across the inner or outer boundaries is much small compared to the GJ value. Since the null surface is formed by the frame-dragging effect, the gap electrodynamics is essentially governed by the frame-dragging effect rather than the magnetic field configurations. This forms a striking contrast to the pulsar outer-magnetospheric gap model, in which the null surface is formed by the convex geometry of the poloidal magnetic field lines. Thus, in a BH magnetosphere, the gap position and its spatial extent, as well as the exerted  $E_{\parallel} = E_{\parallel}(s)$  in the gap, little depend on the magnetic flux function,  $\Psi = A_{\varphi}$ . We thus assume a radial magnetic field on the poloidal plane,  $\Psi = \Psi(\theta)$ .

Because of axial symmetry, the gap electrodynamic structure can be described in the poloidal plane. For simplicity, we assume that the photons propagate radially in this 2-D plane, which is justified if the photons have negligible angular momenta. Provided that the drift motion (e.g., due to toroidal radiation drag in a radial magnetic field, or due to radial gravity in a toroidal magnetic field) is small in the meridional direction, charged particles roughly move along the magnetic field lines in the poloidal plane. In this case, due to relativistic beaming, ultra-relativistic particles emit photons along the instantaneous magnetic field lines; thus, as long as the

poloidal magnetic field is radial, photons propagate on the same magnetic flux surface,  $A_{\varphi} = A_{\varphi}(\theta) = \text{constant}$ . As a result, we can solve the particle equations of motion and the radiative transfer equation along individual radial poloidal magnetic field lines separately.

Even when the magnetic field lines are radial in the poloidal plane, there exists a toroidal magnetic component,  $B_{\varphi}$ , due to retardation, magnetospheric currents, and a frame dragging. It is, however, out of the scope of this paper to restrict the functional form of  $B_{\varphi}(r, \theta)$ , taking account of such effects. In addition,  $B_{\varphi}$  does not affect  $\rho_{\text{GJ}}$  or the propagation direction of particles and photons in the poloidal plane. Thus, we do not specify  $B_{\varphi}$ . Accordingly, instead of computing the curvature radius,  $R_c$ , of the leptons from their 3-D motion in the rotating magnetosphere, we parameterize  $R_c$  when we calculate the curvature emission. Although  $R_c$  affects the spectral shape of curvature emission, it little affects the total luminosity, because the latter is essentially determined by the potential drop within the gap, and because the potential drop is determined by the gap width, which is in turn predominantly determined by the pair production rate of the IC-emitted, VHE photons (not the curvature-emitted, lower energy photons). On these grounds, we adopt  $R_c = r_g$  in the present paper, leaving  $B_{\varphi}$  unconstrained.

##### 4.2. Gap electrodynamics

In the same way as HP16, we solve the stationary gap solution from the set of the Poisson equation for  $\Phi$ , the equations of motion for electrons and positrons, and the radiative transfer equation for the emitted photons.

###### 4.2.1. Poisson equation

To solve the radial dependence of  $\Phi$  in the Poisson equation (15), we introduce the following dimensionless tortoise coordinate,  $\eta_*$ ,

$$\frac{d\eta_*}{dr} = \frac{r^2 + a^2}{\Delta} \frac{1}{r_g}. \quad (18)$$

In this coordinate, the horizon corresponds to the ‘inward infinity’,  $\eta_* = -\infty$ . In this paper, we set  $\eta_* = r/r_g$  at  $r = r_{\text{max}} \equiv 25r_g$ , where the value of  $r_{\text{max}}$  can be chosen arbitrarily and does not affect the results in any ways. The distribution of  $\eta_*$  is depicted as a function of  $r/r_g$  in figure 2. Note that the relationship between  $\eta_*$  and  $r$  does not depend on the colatitude,  $\theta$ .

Since the gap is located near the horizon, we take the limit  $\Delta \ll r_g^2$ . Assuming that  $\Phi$  does not depend on  $\varphi - \Omega_F t$ , that is,  $\Phi = \Phi(r, \theta)$ , we can recast the Poisson equation (15) into the two-dimensional form,

$$\begin{aligned} & - \left( \frac{r^2 + a^2}{\Delta} \right)^2 \frac{\partial^2 \tilde{\Phi}}{\partial \eta_*^2} + \frac{2(r - r_g)(r^2 + a^2)}{\Delta^2/r_g} \frac{\partial \tilde{\Phi}}{\partial \eta_*} \\ & - \frac{r_g^2}{\Delta} \frac{\Sigma}{\sin \theta} \frac{\partial}{\partial \theta} \left( \frac{\sin \theta}{\Sigma} \frac{\partial \tilde{\Phi}}{\partial \theta} \right) \\ & = \left( \frac{\Sigma}{r^2 + a^2} \right)^2 (n_+ - n_- - n_{\text{GJ}}), \end{aligned} \quad (19)$$

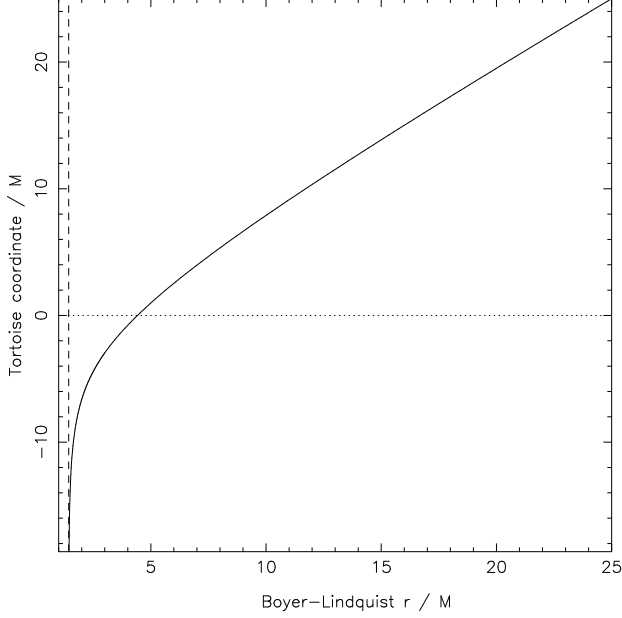


FIG. 2.— Tortoise coordinate versus Boyer-Lindquist radial coordinate. Both axes are normalized by the gravitational radius,  $r_g$ . The BH spin parameter is adopted to be  $a_* = 0.90$ . Vertical dashed line represents the horizon position.

where

$$\tilde{\Phi}(\eta_*) \equiv \frac{c}{2\Omega_F B r_g^2} \Phi(r) \quad (20)$$

denotes the dimensionless non-corotational potential. Dimensionless lepton densities per magnetic flux tube are defined by

$$n_{\pm} \equiv \frac{2\pi c e}{\Omega_F B} N_{\pm}, \quad (21)$$

where the number densities of positrons and electrons,  $N_+$  and  $N_-$ , are computed from the pair production rate at each position (Hirotani & Okamoto 1998; Hirotani & Shibata 1999a,b). Dimensionless GJ charge density per magnetic flux tube is defined by

$$n_{\text{GJ}} \equiv \frac{2\pi c}{\Omega_F B} \rho_{\text{GJ}}. \quad (22)$$

For a radial poloidal magnetic field,  $\Psi = \Psi(\theta)$ , we can compute the acceleration electric field by

$$E_{\parallel} \equiv -\frac{\partial \Phi}{\partial r} = -r_g \frac{\Omega_F B}{c} \frac{r^2 + a^2}{\Delta} \frac{\partial \tilde{\Phi}}{\partial \eta_*}. \quad (23)$$

Without loss of any generality, we can assume  $F_{\theta\varphi} > 0$  in the northern hemisphere. In this case, a negative  $E_{\parallel}$  arises in the gap, which is consistent with the direction of the global current flow pattern.

Equation (16) shows that  $\rho_{\text{GJ}}$  is essentially determined by  $B^r$ , rather than  $B^{\theta}$ , near the horizon. In a stationary and axisymmetric magnetosphere, equation (16) becomes

$$\rho_{\text{GJ}} \propto \partial_r(GF_{\varphi r}) + \frac{1}{\Delta} \partial_{\theta}(GF_{\varphi\theta}), \quad (24)$$

where  $G \equiv (A \sin \theta / \Sigma)(\Omega_F - \omega)$ . Since  $G$ ,  $F_{\varphi r}$ , and  $F_{\varphi\theta}$  are well-behaved at the horizon, we find that the second term dominates the first one at  $\Delta \rightarrow 0$ . Therefore, although the null surface itself is formed by the *frame-dragging* effect, the radial component of the magnetic

field essentially determines  $\rho_{\text{GJ}}$  near the horizon owing to the *redshift* effect.

#### 4.2.2. Leptonic densities

We next consider  $n_-$  and  $n_+$  in equation (19). Because of  $E_{\parallel} < 0$ , electrons are accelerated outwards, while positrons inwards. As a result, as long as there is no current injection across either outer or inner boundaries, charge density,  $n_+ - n_-$ , becomes negative (or positive) at the outer (or inner) boundary. In a stationary gap,  $E_{\parallel}$  should not change sign in it. In a vacuum gap, a positive (or a negative)  $-n_{\text{GJ}}$  near the outer (or inner) boundary makes  $\partial_r E_{\parallel} > 0$  (or  $\partial_r E_{\parallel} < 0$ ), thereby closing the gap. In a non-vacuum gap, the right-hand side of equation (19) should become positive (or negative) near the outer (or inner) boundary so that the gap may be closed. Therefore,  $|n_+ - n_-|$  should not exceed  $|n_{\text{GJ}}|$  at either boundary. At the outer boundary, for instance, we can put

$$(n_+ - n_-)|_{r=r_2} = -n_-(r=r_2) = j n_{\text{GJ}}(r=r_2), \quad (25)$$

where the dimensionless parameter  $j$  should be in the range,  $0 \leq j \leq 1$ , so that the gap solution may be stationary. Since  $F_{\theta\varphi} > 0$  is assumed, it is enough to consider a positive  $j$ . If  $j = 1$ , there is no surface charge at the outer boundary. However, if  $j < 1$ , the surface charge results in a jump of  $\partial_r E_{\parallel}$  at the outer boundary. That is, the parameter  $j$  specifies the strength of  $\partial_r E_{\parallel}$  at the outer boundary. Thus, the inner boundary position,  $r = r_1$ , is determined as a free boundary problem by this additional constraint,  $j$ . The outer boundary position,  $r = r_2$ , or equivalently the gap width  $w = r_2 - r_1$ , is constrained by the gap closure condition (§ 4.2.6).

It is noteworthy that the charge conservation ensures that the dimensionless current density (per magnetic flux tube),  $J_c \equiv -n_+ - n_-$  conserves along the flowline. At the outer boundary, we obtain

$$J_c = -n_-(r=r_2) = j n_{\text{GJ}}(r=r_2). \quad (26)$$

Thus,  $j$  specifies not only  $\partial_r E_{\parallel}$  at the outer boundary, but also the conserved current density,  $J_c$ .

In general, under a given electro-motive force exerted in the ergosphere,  $J_c$  should be constrained by the global current flow pattern, which includes an electric load at the large distances where the force-free approximation breaks down and the trans-magnetic-field current gives rise to the outward acceleration of charged particles by Lorentz forces (thereby converting the Poynting flux into particle kinetic energies). However, we will not go deep into the determination of  $J_c$  in this paper, because we are concerned with the acceleration processes near the horizon, not the global current closure issue. Note that  $w$  (or  $r_2$ ) is essentially determined by  $\dot{m}$ ; thus,  $j$  and  $\dot{m}$  give the actual current density  $(\Omega_F B / 2\pi) J_c$ , where  $B$  should be evaluated at each position. On these grounds, instead of determining  $J_c$  by a global requirement, we treat  $j$  as a free parameter in the present paper.

It may be worth mentioning, in passing, that we may not have to consider a time-dependent solution, which may be obtained when  $j > 1$  as in pulsar polar-cap models (Harding et al. 1978; Daugherty & Harding 1982; Dermer 1994). In the polar cap model, the absence of the null surface results in a non-stationary gap solution

(Timokhin 2010; Timokhin & Arons 2013, 2015). However, in the pulsar outer gap models (Zhang & Cheng 1997; Romani, R. & Watters 2010; Takata et al. 2004; Wang et al. 2011; Hirotani 2015) or in the present BH gap model, the existence of the null surface leads to a formation of a stationary gap around this surface. We thus adopt  $0 \leq j \leq 1$  and consider a stationary gap solution.

#### 4.2.3. Particle motion

Let us describe the motion of electrons and positrons. For simplicity, we assume that the distribution functions of electrons and positrons are mono-energetic. We evaluate the Lorentz factors of electrons (or positron) by the motion of a test particle injected across the inner (or the outer) boundary of the gap. For example, an injected test electron is accelerated by a negative  $E_{\parallel}$  outwards and loses the kinetic energy via curvature and IC processes. The former, curvature radiation rate (per particle) is computed by the standard synchrotron emission formula with the gyration radius replaced with  $R_c$  (Rybicki & Lightman 1979). The latter, IC radiation rate is computed by multiplying the scattering probability (per unit time) and the scattered photon energy. Thus, the particle Lorentz factor saturates at the curvature- or IC-limited value, whichever smaller.

#### 4.2.4. Radiative transfer equation

Throughout this paper, we assume that all photons are emitted with vanishing angular momenta. In this case, photons propagate on a constant- $\theta$  surface; thus, the radiative transfer equation is solved one-dimensionally along the radial magnetic field lines on the poloidal plane. These primary leptons emit photons via curvature and IC processes both inside and outside the gap. For the details of how to compute the emissivities of curvature and IC processes, see §§ 4.2 and 4.3 of HP16.

Some portions of the photons are emitted above 10 TeV via IC process. A significant fraction of such hard  $\gamma$ -rays are absorbed, colliding with the RIAF soft photons. If such collisions take place within the gap, the created electrons and positrons polarize to be accelerated in opposite directions, becoming the primary leptons. If the collisions take place outside the gap, the created, secondary pairs migrate along the magnetic field lines to emit photons via IC and synchrotron processes. Some of such secondary IC photons are absorbed again to materialize as tertiary pairs, which emit tertiary photons via synchrotron and IC processes, eventually cascading into higher generations. As a representative model of the RIAF, we adopt the analytic solution of the advection-dominated accretion flow (ADAF) obtained by Mahadevan (1997).

We assume that the ADAF soft photon specific intensity is isotropic in the zero-angular-momentum observer (ZAMO). This assumption simplifies the calculations of photon-photon pair production and IC scatterings, because photons are assumed to be emitted by leptons with vanishing angular momenta. To calculate the flux of ADAF photons, we assume that their number density is homogeneous and becomes  $L_{\text{ADAF}}/(4\pi R_{\text{min}}^2 c)$  within  $r < R_{\text{min}}$ , where  $L_{\text{ADAF}}$  denotes the ADAF luminosity given by Mahadevan (1997). We assume that the ADAF luminosity becomes  $L_{\text{ADAF}}$  at  $r = R_{\text{min}}$ . Outside this

radius,  $r > R_{\text{min}}$ , we assume that their number density decreases by  $r^{-2}$  law. This treatment may be justified, because the submillimeter-IR photons, which most effectively work both for pair production and IC scatterings, are emitted from the inner-most region of the ADAF.

#### 4.2.5. Boundary conditions

We solve the gap in the 2-D poloidal plane. We assume a reflection symmetry with respect to the magnetic axis. Thus, we put  $\partial_{\theta}\tilde{\Phi} = 0$  at  $\theta = 0$ . We assume that the polar funnel is bounded at a fixed colatitude,  $\theta = \theta_{\text{max}}$  and impose that this lower-latitude boundary is equipotential and put  $\tilde{\Phi} = 0$  at  $\theta = \theta_{\text{max}}$ .

Both the outer and inner boundaries are treated as free boundaries. Their positions are determined by the two conditions, the value of  $j$  along each magnetic field line (specified by  $\Psi$ ), and the gap closure condition (to be described in § 4.2.6). For simplicity, we assume that  $j$  is constant for  $\Psi$ . At the outer boundary,  $\partial_r E_{\parallel} = -\partial_r^2 \Phi$  is specified by  $j$ . At the inner boundary, we impose  $E_{\parallel} = -\partial_r \Phi = 0$ . We assume that electrons, positrons or photons are not injected across either the outer or the inner boundaries.

#### 4.2.6. Gap closure condition

The set of Poisson and radiative-transfer equations are solved together with the terminal Lorentz factor  $\gamma$  and the  $n_{\pm}$  obtained by the local pair production rate. Unlike HP16, we discard the reflection symmetry (along radial magnetic field lines) with respect to the null-charge surface, and explicitly consider the asymmetric distribution of  $E_{\parallel}$ ,  $\gamma$  and  $n_{\pm}$ , and the photon specific intensity at each point  $r$ . Accordingly, the gap closure condition should be modified as  $\mathcal{M}_{\text{in}}\mathcal{M}_{\text{out}} = 1$ , where  $\mathcal{M}_{\text{in}}$  and  $\mathcal{M}_{\text{out}}$  denote the multiplicity (eq. [41] of HP16) associated with the incoming and out-going leptons, respectively. See Hirotani (2013) for a detailed treatment of the asymmetric multiplicities,  $\mathcal{M}_{\text{in}} \neq \mathcal{M}_{\text{out}}$ .

### 5. GAP SOLUTIONS

In § 2, we examined the upper limits of the BH gap luminosity, imposing the charge-starvation condition (eq. [4]) that requires the ADAF to be less luminous so that their MeV photons may not produce pairs above the GJ density. In this section, solving the gap electrodynamics by the method described in § 4 for various BH masses, we demonstrate that the gap becomes most luminous when the gap longitudinal width becomes much greater than the horizon radius, and that there is a lower-limit accretion rate below which a stationary pair-production cascade cannot be maintained within the gap.

Throughout this paper, we assume a radial poloidal magnetic field,  $\Psi = \Psi(\theta) \propto -\cos\theta$ . The magnitude of  $\Psi$  is adjusted so that  $B = B_{\text{eq}}$  (eq. [2]) may be satisfied at  $r = 2r_g$ . Assuming that the poloidal magnetic components dominate the toroidal one, we put  $B(r) = B_{\text{eq}}(r/2r_g)^{-2}$  and compute the synchrotron emission outside the gap. Unless explicitly mentioned, we adopt  $a = 0.90r_g$ ,  $\Omega_F = 0.50\omega_H$ ,  $R_{\text{min}} = 6r_g$ ,  $j = 0.7$ , and  $R_c = r_g$ . To solve the Poisson equation (19), we set the meridional boundary at  $\theta = \theta_{\text{max}} = 60^\circ$ . We assume that the entire system is axisymmetric with respect to the rotation axis, which coincides with the magnetic axis.

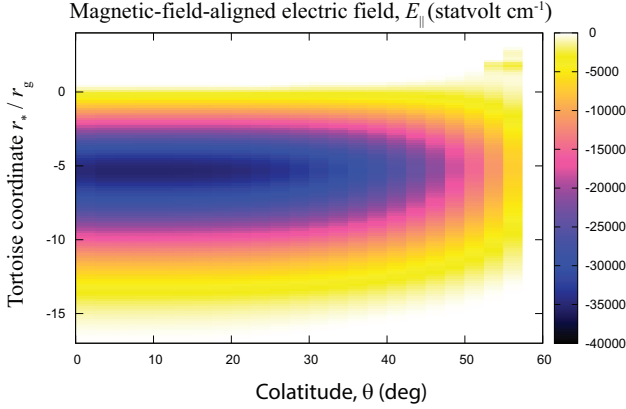


FIG. 3.— Acceleration electric field (statvolt  $\text{cm}^{-1}$ ) on the poloidal plane. The abscissa denotes the magnetic colatitudes,  $\theta$ , in degrees, where 0 (i.e., the ordinate) corresponds to the magnetic axis. The ordinate denotes the dimensionless tortoise coordinate, where  $-\infty$  corresponds to the event horizon. The gap is solved for a black hole with  $M = 10M_\odot$  and  $a_* = 0.9$ . Dimensionless accretion rate is chosen to be  $\dot{m} = 1.00 \times 10^{-4}$ .

### 5.1. The case of stellar-mass BHs

Let us first examine the case of  $M = 10M_\odot$ . We begin with describing the 2-D distribution of the  $E_\parallel$  in § 5.1.1, and demonstrate that the gap emission becomes strongest within the colatitude,  $\theta < 38^\circ$  along the magnetic axis in § 5.1.2. Then in § 5.1.3–§ 5.1.4, we examine the lepton densities and acceleration electric field. Adopting a distance of 1 kpc, we present the expected spectra of gap emissions in § 5.1.5, and examine its dependence on  $j$ ,  $a_*$ , and  $\Omega_F$  in §§ 5.1.7–5.1.9. Finally, in § 5.1.10, we demonstrate that the magnetosphere becomes entirely force-free (except for the gap region) by the cascaded pairs outside the gap.

#### 5.1.1. Electric field along the magnetic field lines

We first present the distribution of the magnetic-field-aligned electric field on the poloidal plane. In figure 3, we plot  $E_\parallel$  (in statvolt  $\text{cm}^{-1}$ ) as a function of the dimensionless tortoise coordinate,  $\eta_*$ , and the magnetic colatitude,  $\theta$  (in degrees), for  $\dot{m} = 1.00 \times 10^{-4}$ .

We also plot  $E_\parallel$  at six discrete colatitudes in figure 4. It follows that the  $E_\parallel(\eta_*)$  distribution little changes in the polar region within  $\theta < 38^\circ$ .

#### 5.1.2. Gap emission versus colatitudes

We next compare the  $\gamma$ -ray spectra of a BH gap emission as a function of the colatitude,  $\theta$ . In figure 5, we compare the SEDs at the same six discrete  $\theta$ 's as in figure 4. It follows that the gap emission becomes most luminous if we observe the gap with a viewing angle  $\theta < 38^\circ$ . This conclusion is unchanged if we adopt different BH masses or spins. In what follows, we therefore adopt  $\theta = 0$  as the representative colatitude to estimate the maximum  $\gamma$ -ray flux of BH gaps.

#### 5.1.3. Created lepton densities

We plot the solved lepton densities at five discrete  $\dot{m}$  in figure 6. Since  $E_\parallel$  is negative, electrons are accelerated outwards while positrons inwards. Thus, the dimensionless electronic density (solid curve),  $n_-$ , per magnetic flux tube, increases outwards, while the positronic one

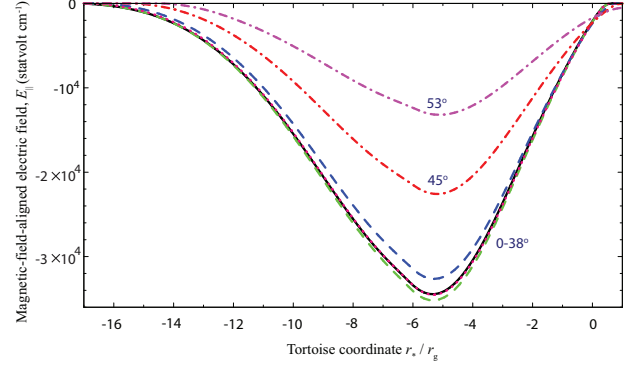


FIG. 4.— Acceleration electric field at six discrete colatitudes,  $\theta$ , as a function of the dimensionless tortoise coordinate,  $\eta_*$ , for  $\dot{m} = 1.00 \times 10^{-4}$ . The values of  $E_\parallel(\eta_*, \theta)$  in figure 3 is plotted at six discrete  $\theta$ 's: the black solid, green dashed, blue dashed, magenta dotted, red dash-dotted, and purple dash-dotted curves denote the  $E_\parallel$  at  $\theta = 0^\circ, 15^\circ, 30^\circ, 37.5^\circ, 45^\circ$ , and  $52.5^\circ$ , respectively.

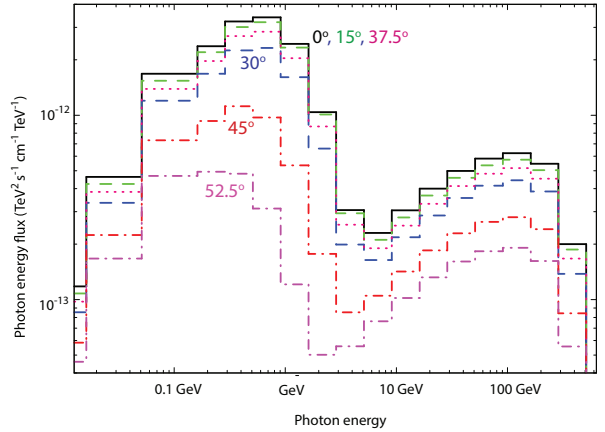


FIG. 5.— Spectral energy distribution (SED) of the emission from a black hole (BH) gap at six discrete colatitudes,  $\theta$ , at a distance of 1 kpc. The gap is solved for a black hole with  $M = 10M_\odot$  and  $a_* = 0.9$ . The dimensionless accretion rate is fixed at  $\dot{m} = 1.00 \times 10^{-4}$ . The six lines correspond to the same  $\theta$ 's as in figure 4.

(dashed curve),  $n_+$ , decreases outwards. Note that the abscissa,  $r - r_0$ , is converted from the tortoise coordinate to the Boyer-Lindquist radial coordinate for presentation purpose. Thus,  $r - r_0 = 0$  corresponds to the null-charge surface. These solved  $n_\pm(r, \theta)$  are used to compute the real charge density  $\rho = (\Omega_F B / 2\pi c)(n_+ - n_-)$  at each position, which is necessary to solve  $E_\parallel$  on the poloidal plane. We continue iterations until  $n_\pm(\eta_*, \theta)$ ,  $E_\parallel(\eta_*, \theta)$ , and the photon specific intensity saturate.

#### 5.1.4. Acceleration electric field

As  $\dot{m}$  decreases, the reduced ADAF near-IR photon field leads to less efficient pair production, thereby resulting in an extended gap to sustain the externally required current density,  $j$ , per magnetic flux tube. We plot  $E_\parallel(r, \theta = 0)$  for five discrete  $\dot{m}$ 's in figure 7. The cyan, blue, green, black, and red curves correspond to the cases of  $\dot{m} = 10^{-3.0}, 10^{-3.5}, 10^{-4.0}, 10^{-4.125}$ , and  $10^{-4.25}$ , respectively; that is, same as figure 6. Integrating  $E_\parallel$  over the gap width, we obtain the potential drop at each  $\dot{m}$ . It becomes  $-6.3 \times 10^{11}$  V,  $-3.9 \times 10^{12}$  V,

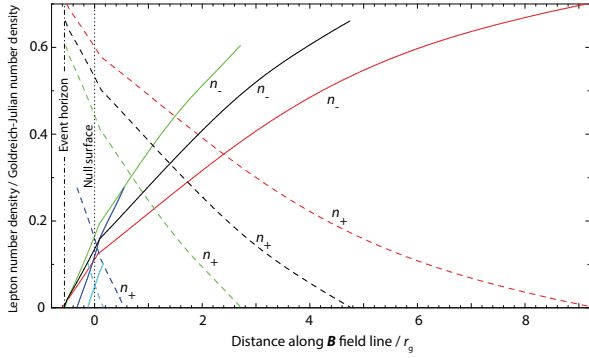


FIG. 6.— Spatial distribution of the electronic (solid) and positronic (dashed) densities per magnetic flux tube as a function of the distance,  $r - r_0$ , from the null-charge surface, in the Boyer-Lindquist radial coordinate (in  $r_g \equiv GMc^{-2}$  unit). The gap is solved for a black hole with  $M = 10M_\odot$  and  $a_* = 0.9$ . Viewing angle is chosen to be  $\theta = 0$ . The cyan, blue, green, black, and red curves represent the solutions for  $\dot{m} = 1.00 \times 10^{-3}$ ,  $3.16 \times 10^{-4}$ ,  $1.00 \times 10^{-4}$ ,  $7.49 \times 10^{-5}$ , and  $5.62 \times 10^{-5}$ , respectively. The vertical dashed line at  $r - r_0 = 0$  shows the null surface position.

$-2.5 \times 10^{13}$  V,  $-4.2 \times 10^{13}$  V, and  $-6.3 \times 10^{13}$  V, for  $\dot{m} = 10^{-3.0}$ ,  $10^{-3.5}$ ,  $10^{-4.0}$ ,  $10^{-4.125}$ , and  $10^{-4.25}$ , respectively. Thus, the potential drop increases with decreasing  $\dot{m}$  because of the increased gap width,  $w \equiv r_2 - r_1$ . More specifically, as the accretion rate reduces, the decreased ADAF near-IR photon field results in a less effective pair production for the gap-emitted IC photons, thereby increasing the mean-free path for two-photon collisions. Since  $w$  essentially becomes the pair-production mean-free path divided by the number of photons emitted by a single electron above the pair production threshold energy (Hirotani & Okamoto 1998), the reduced pair production leads to an extended gap along the magnetic field lines. As a result, the smaller  $\dot{m}$  is, the greater the potential drop becomes.

As  $w$  increases, the trans-field derivative begins to contribute in the Poisson equation (19). As a result, the  $E_\parallel$  distribution shifts outwards, in the same way as in pulsar outer-magnetospheric gaps (fig. 12 of Hirotani & Shibata 1999a). That is, a pulsar outer gap extends from the null surface to (or beyond) the light cylinder because the transverse thickness is limited by the efficient screening of  $E_\parallel$  due to the trans-field propagation in concave poloidal magnetic field lines, whereas a BH gap shifts from the null surface towards the outer light surface because the longitudinal width becomes comparable to the transverse thickness when the accretion rate is small.

Let us briefly examine how the gap width,  $w$ , is affected when the ADAF soft photon field changes. In figure 8, we plot the gap inner and outer boundary positions as a function of  $\dot{m}$ , where the ordinate is converted into the Boyer-Lindquist radial coordinate. It follows that the gap inner boundary (solid curve,  $r = r_1$ ), infinitesimally approaches the horizon (dash-dotted horizontal line,  $r = r_H$ ), while the outer boundary (dashed curve,  $r = r_2$ ) moves outwards, with decreasing  $\dot{m}$ . Below the accretion rate  $\dot{m} \sim \dot{m}_{\text{low}} = 2 \times 10^{-4}$ , the outer boundary moves rapidly away from the horizon with decreasing  $\dot{m}$ , so that the required current density,  $j = 0.7$ , may be pro-

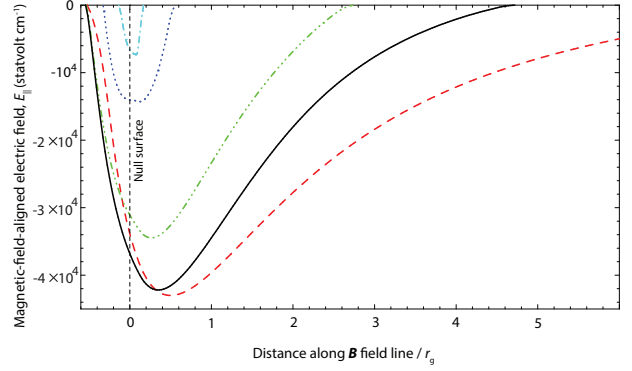


FIG. 7.— Spatial distribution of the magnetic-field-aligned electric field,  $E_\parallel$ , for five discrete accretion rates. The gap is solved for a black hole with  $M = 10M_\odot$  and  $a_* = 0.9$ . Each color corresponds to the same cases of  $\dot{m}$ 's as in figure 6. The vertical dashed line shows the null surface position.

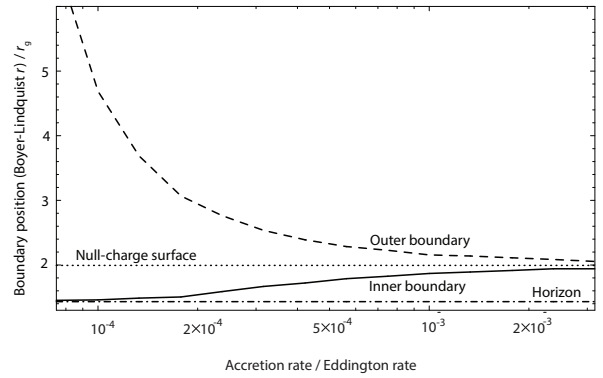


FIG. 8.— Spatial extent of the gap along the radial poloidal magnetic field line as a function of the dimensionless accretion rate. The gap is solved for a black hole with  $M = 10M_\odot$  and  $a_* = 0.9$ . Thick solid and dashed curves denote the position of the inner and the outer boundaries of the gap, in the unit of the gravitational radius,  $r_g \equiv GMc^{-2}$ . These boundary positions (in the ordinate) are transformed from the tortoise coordinate into the Boyer-Lindquist coordinate. The horizontal dash-dotted line shows the horizon radius, whereas the horizontal dotted line does the null surface position on the magnetic axis,  $\theta = 0$ .

duced within the gap under a diminished ADAF photon field. At  $\dot{m} = 5.62 \times 10^{-5}$ , and  $4.21 \times 10^{-5}$ , the outer boundary is located at  $r_2 = 9.35r_g$  and  $28.64r_g$ . We consider that the solution with  $r_2 > 10r_g$  may not have significant physical meaning, because the funnel boundary with the equatorial disk will deviate from a conical shape beyond this radius (McKinney & Gammie 2004; Hirose et al. 2004; Krolik et al. 2005; McKinney 2006; McKinney et al. 2012; O’ Riordan 2016). We thus define the lower-limit accretion rate,  $\dot{m}_{\text{low}}$  when  $r_2$  exceeds  $10r_g$  in this paper. Indeed, at further lower accretion rate,  $\dot{m} \leq 3.16 \times 10^{-5}$ , we fail to find a 2-D gap solution, because the weak ADAF photon field can no longer sustain the current density,  $j = 0.7$ , per magnetic flux tube. Thus, we obtain  $\dot{m}_{\text{low}} = 5.56 \times 10^{-5}$  for  $M = 10M_\odot$ ,  $a = 0.90r_g$ ,  $\Omega_F = 0.50\omega_H$ , and  $j = 0.7$ , interpolating  $r_2 = r_2(\dot{m})$  and putting  $r_2 = 10r_g$ . Because  $r_2$  rapidly increases near  $\dot{m} \sim \dot{m}_{\text{low}}$ , the value of  $\dot{m}_{\text{low}}$  little depends on whether we define it by e.g.,  $r_2 = 10r_g$  or  $r_2 = 20r_g$ .

### 5.1.5. Spectrum of gap emission

The predicted photon spectra are depicted in figure 9 for the same set of  $\dot{m}$  as in figures 6 and 7. The thin

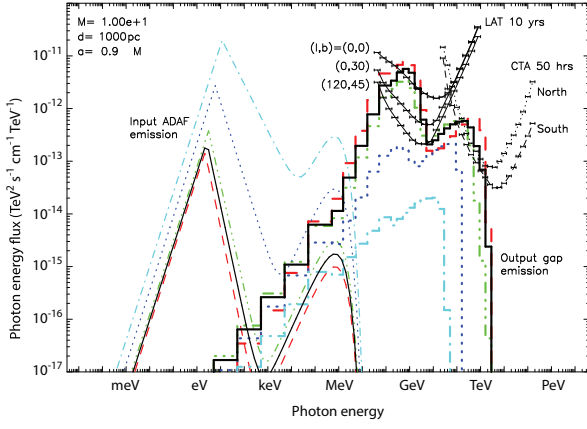


FIG. 9.— SED of the gap emission for a stellar-mass black hole with  $M = 10M_{\odot}$  and  $a_* = 0.9$ , for five discrete dimensionless accretion rates,  $\dot{m}$ 's at 1 kpc. The thin curves denote the input ADAF spectra, while the thick lines do the output gap spectra. Each color corresponds to the same cases of  $\dot{m}$ 's as in figures 6–7. The thin solid curves (with horizontal bars) denote the Fermi/LAT detection limits after 10 years observation, while the thin dashed and dotted curves (with horizontal bars) denote the CTA detection limits after a 50 hours observation. Magnetic field strength is assumed to be the equipartition value with the plasma accretion.

curves on the left denote the input ADAF spectra, while the thick lines on the right do the output spectra from the gap. We find that the emitted flux increases with decreasing  $\dot{m}$ , because the potential drop in the gap increases with decreasing  $\dot{m}$ . The spectral peak around GeV is due to the curvature emission, while that around TeV is due to the IC scatterings. Provided that the distance is within several kpc, these HE and VHE fluxes appear above the Fermi/LAT detection limits (three thin solid curves labeled with “LAT 10 yrs”),<sup>1</sup> and the CTA detection limits (dashed and dotted curves labeled with “CTA 50 hrs”).<sup>2</sup> Since BH transients spend bulk of their time in a (very weakly accreting) quiescent state (e.g., Miller-Jones et al. 2011; Plotkin et al. 2013), it is possible for near-by BH transients to exhibit detectable BH emissions. For example, in HE, the flaring photons will be detectable if the duty cycle of the flaring activities is not too small (e.g.,  $> 0.1$ ).

We plot the individual emission components in figure 10, picking up the case of  $\dot{m} = 7.49 \times 10^{-5}$  (i.e., the case of the black solid line in fig. 9). The red dashed line shows the primary curvature component, while the red dash-dotted line the primary IC component. The former component is not absorbed and appear as the spectral peak at several GeV when  $\dot{m} \sim \dot{m}_{\text{low}}$  (i.e., when the gap outer boundary is located at  $r_2 \gg r_g$ ). The latter component is heavily absorbed by the ADAF near-IR photons to be reprocessed as the secondary component (blue dash-dot-dot-dotted line). In this secondary component, IC emission dominates above GeV and the synchrotron component dominates only below this energy. The secondary component above 500 GeV is absorbed again to be reprocess as the tertiary component (purple dotted).

To grasp the strength of the absorption taking place inside and outside the gap, we examine the optical depth

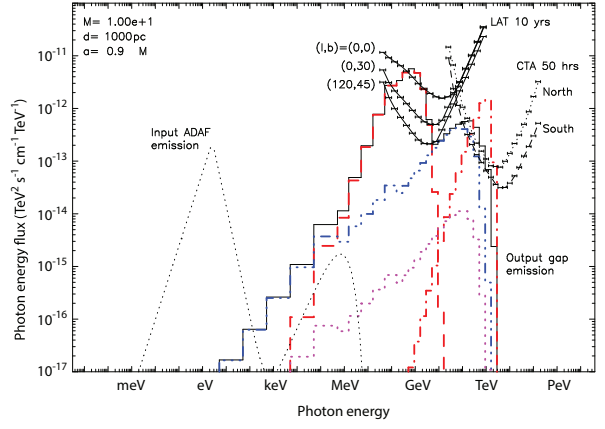


FIG. 10.— Similar figure as fig. 9, but only the case of  $\dot{m} = 7.49 \times 10^{-5}$  is depicted. The thick and thin black curves correspond to the same ones in figure 9. The red dashed and dash-dotted lines denote the primary curvature and inverse-Compton components, respectively. The blue dash-dot-dot-dotted and purple dotted ones do the secondary and tertiary emission via synchrotron and inverse-Compton processes outside the gap.

for photon-photon collisions. For presentation purpose, we compute a representative optical depth for test photons emitted outwards at the gap inner boundary,  $r = r_1$ . With vanishing angular momenta, photons propagate in the  $(r, \theta)$  surface (with constant  $\theta$ ). Thus, the invariant distance,  $ds$ , of a photon path after propagating  $dr$  and  $d\varphi$  in  $r$  and  $\varphi$  coordinates becomes

$$ds^2 = g_{rr}dr^2 + g_{\theta\theta}d\theta^2 = \frac{\Sigma}{\Delta}dr^2 \left[ 1 + O\left(\frac{\Delta \sin^2 \theta}{r_g^2}\right) \right]. \quad (27)$$

Thus, near the pole,  $|\theta| \ll 1$ , and near the horizon,  $\Delta \ll r_g^2$ , we can put  $ds \approx \sqrt{\Sigma/\Delta}dr$ . Integrating the local absorption probability over the photon ray, we can compute the optical depth by

$$\tau(\nu) = \int_{s_1}^{\infty} \frac{d\tau}{ds} ds = \int_{r_1}^{\infty} \sqrt{\frac{\Sigma}{\Delta}} \frac{d\tau}{ds} dr, \quad (28)$$

where  $ds$  coincides with the distance of radial interval,  $dr$ , measured by ZAMO. The radial gradient of the optical depth becomes

$$\frac{d\tau}{ds} = \frac{1}{c} \int_0^1 d\mu' \int_{\nu'_{\text{th}}}^{\infty} \frac{d\sigma_{\gamma\gamma}(\nu', \nu'_s, \mu')}{d\mu'} \frac{dF'_s}{d\nu'_s} d\nu'_s, \quad (29)$$

where the primes denote quantities evaluated by ZAMO;  $\mu'$  is the cosine of the collision angle of two photons,  $\nu'_s$  the soft photon energy, and  $F'_s$  the soft photon number flux. We employ ZAMO here, because the photons are assumed to be emitted with vanishing angular momenta in this paper. The threshold energy is defined by  $\nu'_{\text{th}} = [2/(1 - \mu')](m_e c)^2 / h^2 \nu'$ , where  $h$  means the Planck constant. The photon frequency  $\nu$  (at infinity) is de-redshifted to the ZAMO's value,  $\nu'$  at each altitude,  $r$ . Specifically, the local photon energy,  $h\nu'$ , is related to  $h\nu$ , by  $h\nu' = i(h\nu + m \cdot d\varphi/dt)$ , where  $m$  denotes the photon angular momentum and  $d\varphi/dt$  the local observer's angular frequency in  $dt$ -basis at  $r$ . However, we here have  $m = 0$ , which gives the ZAMO's angular frequency,  $d\varphi/dt = -g_{t\varphi}/g_{\varphi\varphi}$ . The quantity  $i$  is given by the definition of the proper time,  $i^2[g_{tt} + 2g_{t\varphi}d\varphi/dt +$

<sup>1</sup> [https://www.slac.stanford.edu/exp/glast/groups/canda/lat\\_Performance.htm](https://www.slac.stanford.edu/exp/glast/groups/canda/lat_Performance.htm)

<sup>2</sup> <https://portal.cta-observatory.org/CTA-Observatory/performance/SieAssets/SitePages/Home.aspx>

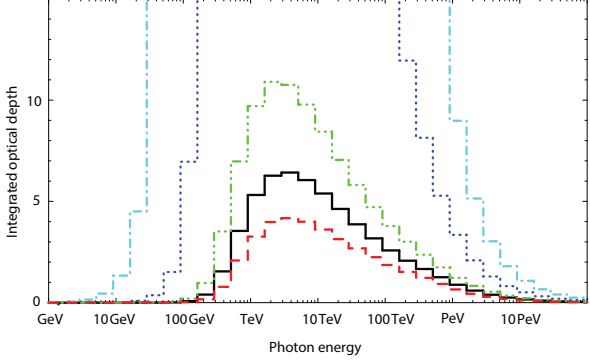


FIG. 11.— Optical depth,  $\tau$ , for photon-photon absorption as a function of the photon energy,  $h\nu$ , at infinity for five  $\dot{m}$ 's. A test photon is supposed to be emitted outwards with zero angular momentum from the gap inner boundary to infinity. The photon energy  $h\nu$  is de-redshifted at each altitude,  $r$ , and the absorption probability gradient  $d\tau/ds$  is integrated from the inner boundary to  $60r_g$ , which is large enough.

$g_{\varphi\varphi}(d\varphi/dt)^2] = -1$ , which reduces to  $\dot{t} = \sqrt{g_{\varphi\varphi}}/\rho_w$  for a ZAMO. Thus, we obtain  $\nu' = \nu\sqrt{g_{\varphi\varphi}}/\rho_w$  as the redshift relation between us and ZAMO. Note that the integral  $\int_{r_H}^r \Delta^{-1/2} dr$  in equation (28) is finite for a finite  $r$ , and that  $dF'_s/d\nu'_s$ , and hence  $d\tau/ds$  vanishes at large distances.

In figure 11, we present  $\tau(\nu)$  for five discrete accretion rates: The five lines correspond to the same cases of  $\dot{m}$ 's as in figures 6, 7, and 9. It follows that the photon-photon absorption optical depth exceeds unity above 16 GeV, 90 GeV, 0.3 TeV, 0.5 TeV, and 0.9 TeV for  $\dot{m} = 1.00 \times 10^{-3}$ ,  $3.16 \times 10^{-4}$ ,  $1.00 \times 10^{-4}$ ,  $7.49 \times 10^{-5}$ , and  $5.62 \times 10^{-5}$ , respectively. The optical depth peaks at several TeV, because the ADAF photon spectrum peaks in near-IR wavelengths for stellar-mass BHs.

It should be stressed that the actual photons are absorbed by smaller optical depths than this figure, because the individual photons are emitted at different positions whose altitudes are always higher than the inner boundary.

#### 5.1.6. Curvature versus Inverse-Compton processes

It is worth examining the relative importance of the curvature and IC processes. In figure 12, we plot the luminosity of the outward curvature-emitted photons as the solid curve, and that of the IC-emitted photons as the dash-dotted one, as a function of  $\dot{m}$ . The outward curvature photons are mostly emitted inside the gap, while the IC photons are emitted both inside and outside the gap. Figure 12 shows that the curvature luminosity exceeds the IC one when  $\dot{m} < 2 \times 10^{-4}$ , or equivalently when the gap extends enough. This is because the curvature power is proportional to  $\gamma^4$ , while the IC power approximately to  $\gamma^0 \sim \gamma^2$ , depending on whether the collisions take place mainly in the extreme Klein-Nishina or the Thomson regime. The IC power also depends on the specific intensity of the soft photon field; thus, its dependence on  $\gamma$  is more complicated than the curvature process.

#### 5.1.7. Luminosity versus created current density

Let us briefly examine the dependence of the spectrum on the created current density,  $j$ . In figure 13, we plot the gap spectra at six discrete  $j$ 's. It follows that the HE emission becomes most luminous when  $0.5 \leq j \leq 0.7$

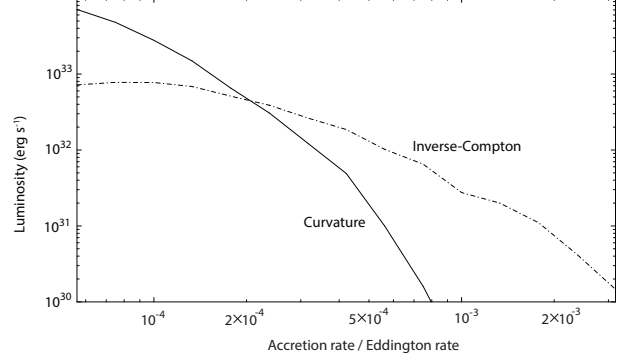


FIG. 12.— Gap luminosity as a function of the dimensionless accretion rate for a stellar-mass black hole with  $M = 10M_\odot$  and  $a_* = 0.9$ . The solid and dash-dotted curves denote the luminosity of the curvature and inverse-Compton processes, respectively.

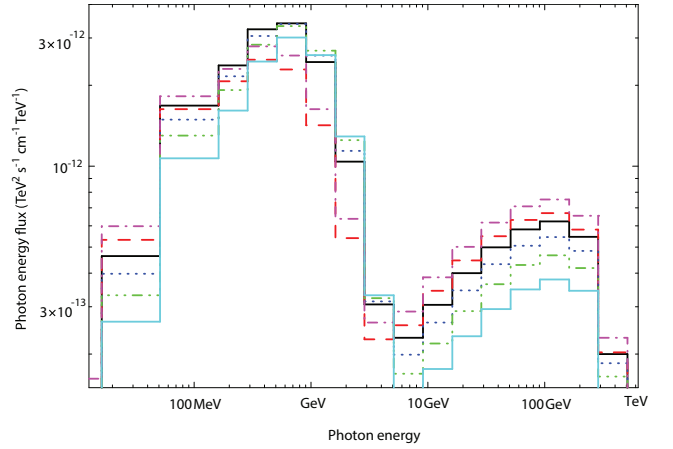


FIG. 13.— SED of the gap emission along the magnetic axis,  $\theta = 0$ , at the distance of 1 kpc, from a BH with  $M = 10M_\odot$  and  $a = 0.9r_g$ . The cyan solid, green dash-dot-dot-dotted, blue dotted, black solid, red dashed, and purple dash-dotted lines correspond to the dimensionless created current densities,  $j = 0.4, 0.5, 0.6, 0.7, 0.8$ , and  $0.9$ , respectively. The accretion rate is fixed at  $\dot{m} = 1.00 \times 10^{-4}$ .

and the VHE one does when  $j \sim 0.9$ . In what follows, we thus adopt  $j = 0.7$  as a compromise to optimize the HE and VHE fluxes. Note that we restrict our argument for  $|j| \leq 1$ , because  $|j| > 1$  would incur a sign reversal of the  $\rho - \rho_{GJ}$  in equation (19), thereby resulting in a sign reversal of  $E_\parallel$  at the outer boundary,  $r = r_2$ , which would violate the present assumption of stationarity.

#### 5.1.8. Luminosity versus BH spin

We next briefly investigate how the spectrum depends on the BH spin parameter,  $a_* = a/r_g$ . In figures 14 and 15, we present the gap spectra for  $a_* = 0.5$  and  $0.998$  when  $\dot{m} = 1.00 \times 10^{-4}$ . It follows that the gap flux increases with increasing BH spin. Thus, we adopt  $a_* = 0.9$  as the representative value in this paper.

#### 5.1.9. Luminosity versus magnetic field rotation

It is numerically suggested that the angular frequency,  $\Omega_F$ , of an accreting BH magnetosphere decreases from  $0.3\omega_H$  in the middle latitudes to  $-0.17\omega_H$  in the higher latitudes (i.e., near the pole) (McKinney et al. 2012). Similar tendency, from  $0.4\omega_H$  to  $-0.2\omega_H$  is, indeed, analytically suggested (Beskin & Zheltoukhov 2013). Thus, in this subsection, we examine a smaller  $\Omega_F$  case. In fig-

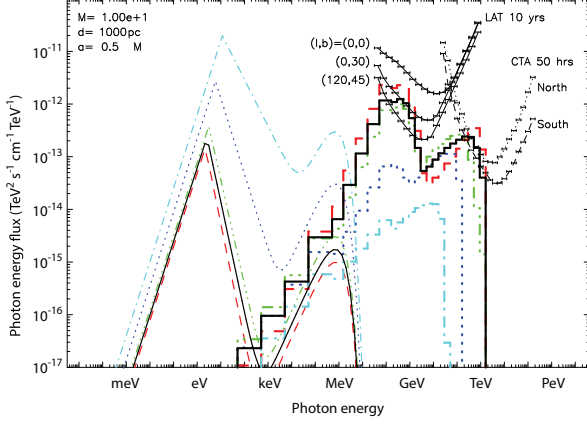


FIG. 14.— Similar figure as figure 9, but the BH spin is chosen to be  $a_* = 0.5$ , while other parameters are the same, including the accretion rate,  $\dot{m}$ .

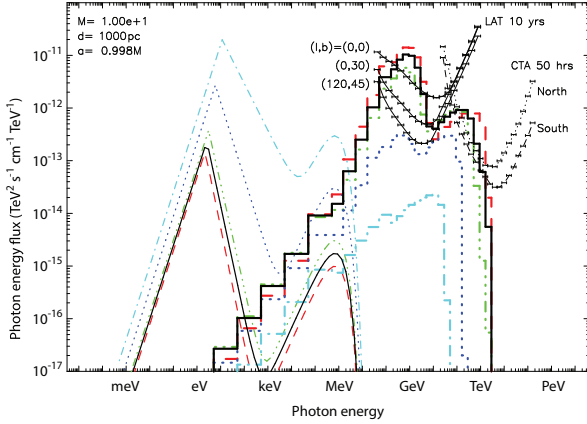


FIG. 15.— Similar figure as figures 9 and 14, but the BH is maximally rotating,  $a_* = 0.998$ . Other parameters are the same as figures 9 and 14, including the accretion rate,  $\dot{m}$ .

ure 16, we plot the SED for  $\Omega_F = 0.20\omega_H$ , keeping other parameters unchanged from figure 9. It follows that the HE flux decreases to about 17 % of the  $\Omega_F = 0.5\omega_H$  case, while the VHE flux is roughly unchanged. The VHE flux changes mildly, because the IC process depends on the lepton Lorentz factor weakly, compared to the curvature process. Note that the BZ power, which is proportional to  $\Omega_F(\omega_H - \Omega_F)$ , reduces to only 64 % of the  $\Omega_F = 0.5\omega_H$  case. It means that the gap becomes less efficient at smaller (in fact, also at greater)  $\Omega_F/\omega_H$  than 0.5. Thus, we adopt  $\Omega_F = 0.5\omega_H$  as the representative value.

#### 5.1.10. Cascaded pairs outside gap

Let us investigate if a force-free magnetosphere is realized outside the gap. We compute the densities of the cascaded pairs within the cutting radius  $r_{\text{cut}} = 60r_g$ , which is well above the gap outer boundary,  $r = r_2$ . In figure 17, we plot the secondary, tertiary, and quaternary pair densities by the red dashed, green dash-dotted, and blue dash-dot-dot-dotted curves, respectively. Here, the secondary pairs denote those cascaded from the primary  $\gamma$ -rays, which are defined to be emitted by the primary electrons or positrons that are accelerated in the gap. The tertiary pairs denote those cascaded from the secondary  $\gamma$ -rays, which are defined to be emitted by these secondary pairs.

It follows that the density of the cascaded pairs exceeds

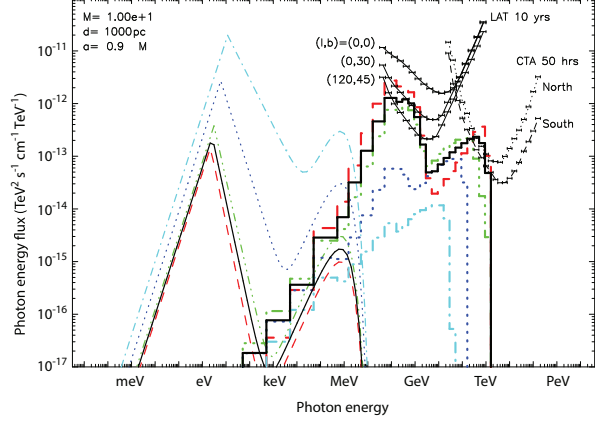


FIG. 16.— Similar figure as figures 9, but the magnetosphere is more slowly rotating,  $\Omega_F = 0.20\omega_H$ . Other parameters are the same, including the accretion rate,  $\dot{m}$ .

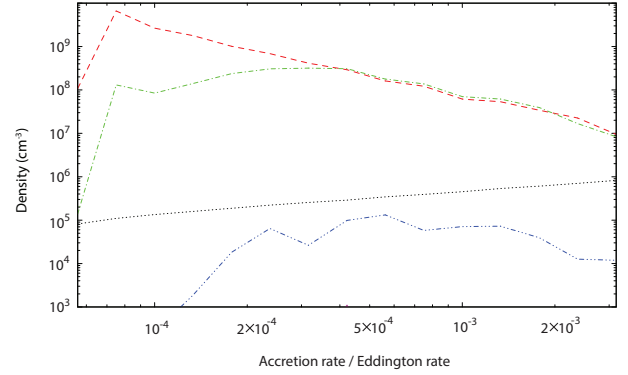


FIG. 17.— Density of the cascaded pairs outside the gap, within radius  $r_2 < r < 60r_g$ , is plotted as a function of  $\dot{m}$  for  $M = 10M_\odot$  and  $a_* = 0.9$ . The red dashed, green dash-dotted, and blue dash-dot-dot-dotted curves denote the densities of the secondary, tertiary, and quaternary pairs, respectively. The black dotted curve shows the Goldreich-Julian charge density, which is volume-averaged within the sphere of  $r = 60r_g$ .

the GJ one (black dotted line), as long as a stationary gap is formed. Thus, the magnetosphere becomes force-free outside the gap, as long as  $\dot{m} > \dot{m}_{\text{low}}$ . This conclusion does not depend on the choice of  $r_{\text{cut}}$ .

In short, gap solutions exist if the dimensionless accretion rate is in the range  $\dot{m}_{\text{low}} < \dot{m} < \dot{m}_{\text{up}}$ . For stellar-mass BHs, the gap emission peaks at several GeV and its maximum flux  $> 10^{-12}$  ergs  $\text{s}^{-1}$  is detectable with *Fermi*/LAT, if the duty cycle of the flaring activity is not too small. The gap luminosity increases with decreasing  $\dot{m}$ , because the gap is dissipating a portion of the BH's spin-down luminosity. This forms a striking contrast to accretion-powered systems, whose luminosity will decrease with decreasing  $\dot{m}$ . The cascaded pairs outside the gap have a greater density than the Goldreich-Julian value; thus, the magnetosphere becomes force-free in the downstream of the gap-generated flow (i.e., outside the gap outer boundary).

#### 5.2. The case of intermediate mass BHs

Let us examine the gap emission from intermediate-mass BHs. We put  $M = 10^3 M_\odot$  and calculate the gap emission for  $a_* = 0.9$  and  $\Omega_F = 0.5\omega_H$ . The predicted spectra become as the top panel in figure 18 for a distance of 10 kpc. It shows that the  $\gamma$ -ray fluxes are detectable

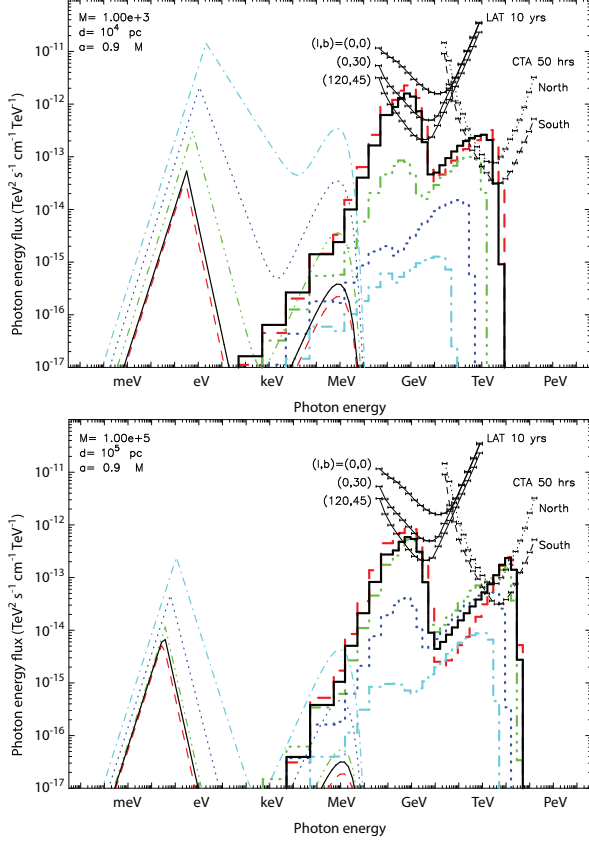


FIG. 18.— *Top panel:* SED of the gap for a BH with  $M = 10^3 M_\odot$ ,  $a_* = 0.9$ , and  $\Omega_F = 0.5\omega_H$ . The distance is assumed to be 10 kpc. The cyan, blue, green, black, and red curves represent the SEDs for  $\dot{m} = 1.00 \times 10^{-3}$ ,  $3.16 \times 10^{-4}$ ,  $1.00 \times 10^{-4}$ ,  $3.16 \times 10^{-5}$ , and  $2.37 \times 10^{-5}$ , respectively. *Bottom panel:* SED for  $M = 10^5 M_\odot$ ,  $a_* = 0.9$ , and  $\Omega_F = 0.5\omega_H$ . The distance is assumed to be 100 kpc. The cyan, blue, green, black, and red curves represent the SEDs for  $1.00 \times 10^{-4}$ ,  $\dot{m} = 3.16 \times 10^{-5}$ ,  $1.00 \times 10^{-5}$ ,  $7.49 \times 10^{-6}$ , and  $5.62 \times 10^{-6}$ , respectively.

in both HE and VHE if an IMBH is located within our galaxy, as long as the accretion rate is in the range,  $2 \times 10^{-5} < \dot{m} < 4 \times 10^{-5}$ .

Since the absolute luminosity of the gap increases with  $M$ , we also compute the SEDs for  $M = 10^5 M_\odot$  (bottom panel of fig. 18), assuming  $d = 100$  kpc. It shows that such a heavy BH is detectable in HE or VHE only when the distance is comparable to or less than 100 kpc.

The curvature and IC luminosities are plotted as a function of  $\dot{m}$  in figure 19. It shows that the curvature process works stronger than the IC when  $\dot{m} < 6 \times 10^{-5}$  for  $M = 10^3 M_\odot$ , and when  $\dot{m} < 1.5 \times 10^{-5}$  for  $M = 10^5 M_\odot$ .

We examine if a force-free magnetosphere is sustained. Figure 20 shows the densities of the pairs cascaded between  $r_2$  and  $60r_g$ . It follows that the density of the cascaded pairs exceeds the GJ one for both  $M = 10^3 M_\odot$  and  $M = 10^5 M_\odot$ .

### 5.3. The case of super-massive BHs

Next, let us examine super-massive BHs. We present the acceleration electric field in § 5.3.1, gap spectrum in § 5.3.2, and cascaded pair densities in § 5.3.3. We briefly examine the dependence on the soft photon density in § 5.3.4.

#### 5.3.1. Acceleration electric field

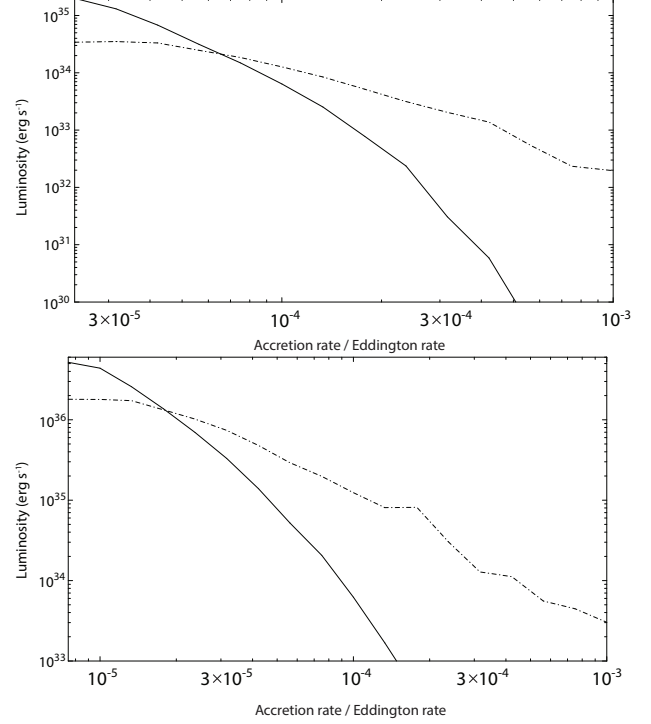


FIG. 19.— *Top panel:* Gap luminosity as a function of the dimensionless accretion rate for a BH with  $M = 10^3 M_\odot$ ,  $a_* = 0.9$ , and  $\Omega_F = 0.5\omega_H$ . The solid and dash-dotted curves denote the luminosity of the curvature and inverse-Compton processes, respectively. *Bottom panel:* Similar figure as the top panel but for  $M = 10^5 M_\odot$ .

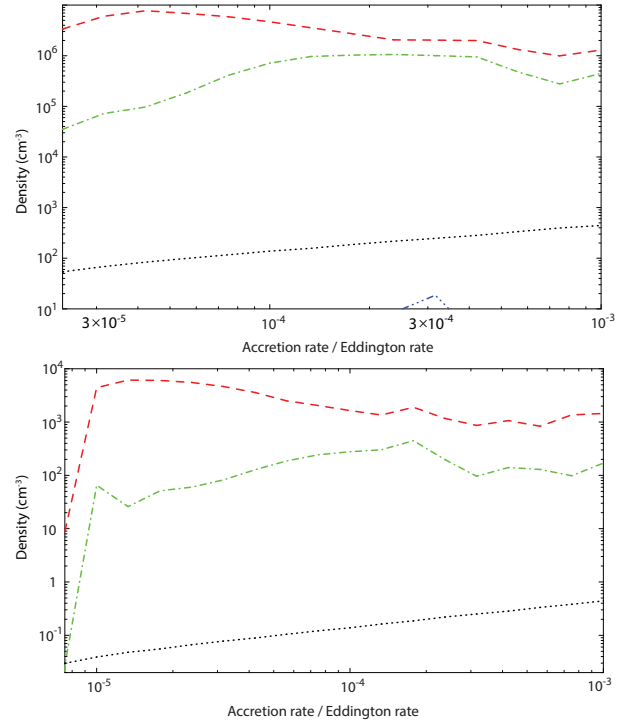


FIG. 20.— Similar figure as figure 17, but for a BH with  $M = 10^3 M_\odot$  (top panel) and  $M = 10^5 M_\odot$  (bottom panel);  $a_* = 0.9$  and  $\Omega_F = 0.5\omega_H$  are unchanged. The dashed and dash-dotted curves denote the densities,  $N_\pm$ , of the secondary and tertiary pairs, while the dotted one the GJ value,  $N_{GJ}$ .

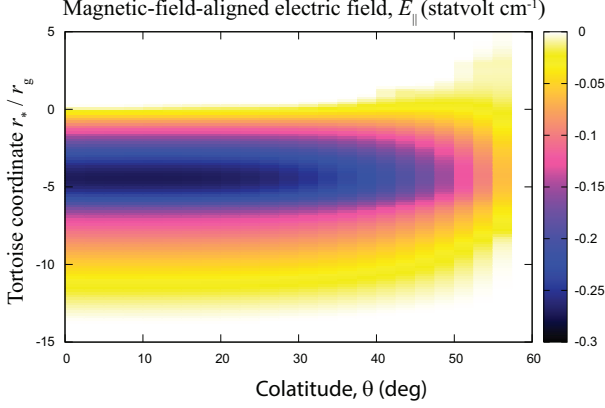


FIG. 21.— Similar figure as figure 4, but for  $M = 10^9 M_\odot$ . The dimensionless accretion rate is chosen to be  $\dot{m} = 1.00 \times 10^{-6}$ .

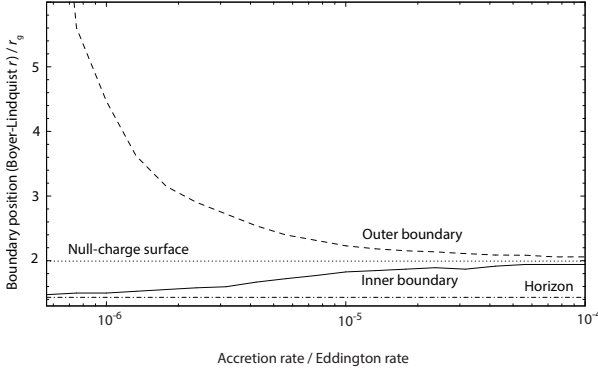


FIG. 22.— Similar figure as figure 8, but for a super-massive black hole with  $M = 10^9 M_\odot$  and  $a_* = 0.9$ .

Choosing a typical mass of  $M = 10^9 M_\odot$ , we plot  $E_\parallel(\eta_*, \theta)$  distribution in figure 21, whose ordinate is the dimensionless tortoise coordinate,  $\eta_*$ . Comparing with figure 3, we find that the essential behavior of  $E_\parallel$  is unchanged from the case of  $M = 10 M_\odot$ . In Boyer-Lindquist radial coordinate, the gap outer and inner boundaries distribute as a function of  $\dot{m}$  as depicted in figure 22. The gap outer boundary is located at  $r_2 = 5.60 r_g$  and  $r_2 = 10.32 r_g$  at  $\dot{m} = 7.49 \times 10^{-7}$  and  $5.62 \times 10^{-7}$ , respectively; thus, we obtain  $\dot{m}_{\text{low}} = 5.75 \times 10^{-7}$  for  $M = 10^9 M_\odot$ ,  $a = 0.90 r_g$ ,  $\Omega_F = 0.50 \omega_H$ , and  $j = 0.7$ . Figure 22 shows that the gap longitudinal width becomes comparable or greater than  $r_g$  when the accretion rate reduces to  $\dot{m} < 2 \times 10^{-6}$ , whereas it is realized when  $\dot{m} < 2 \times 10^{-4}$  for a stellar-mass case (fig. 8). It also follows that the gap outer boundary shifts outwards with decreasing  $\dot{m}$ , in the same manner as the  $M = 10 M_\odot$  case.

### 5.3.2. Spectrum of gap emission

Figure 23 shows the gap spectra as the thick lines for five discrete  $\dot{m}$ 's, assuming a luminosity distance of 10 Mpc. When the accretion rate is in the range  $5.6 \times 10^{-7} < \dot{m} < 10^{-6}$ , we find that the gap emission will be marginally detectable with CTA, if the source is located in the southern sky.

The emission components are depicted in figure 24 for  $\dot{m} = 7.49 \times 10^{-7}$ . Since  $\dot{m}$  is much smaller than the stellar-mass cases, the absorption optical depth decreases accordingly; as a result, most of the primary IC com-

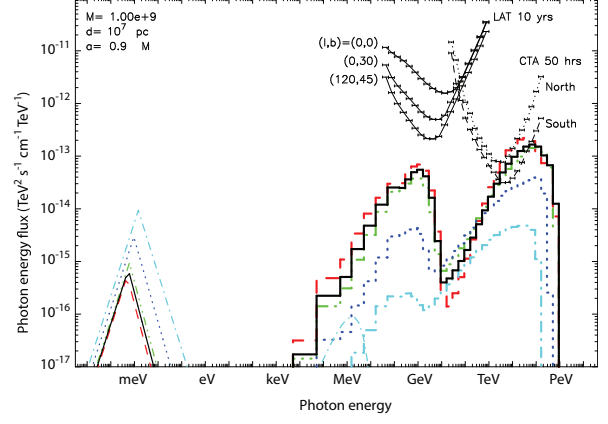


FIG. 23.— SED of the gap for a super-massive BH with  $M = 10^9 M_\odot$  and  $a_* = 0.9$  at 10 Mpc. The cyan, blue, green, black, and red curves represent the SEDs for  $\dot{m} = 1.00 \times 10^{-5}$ ,  $3.16 \times 10^{-6}$ ,  $1.00 \times 10^{-6}$ ,  $7.49 \times 10^{-7}$ , and  $5.62 \times 10^{-7}$ , respectively.

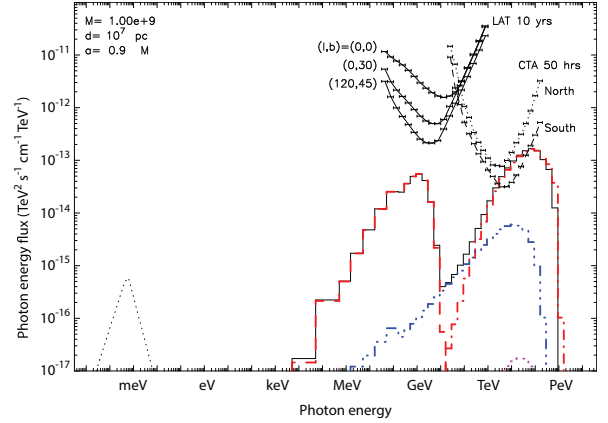


FIG. 24.— Similar figure as fig. 23, but only the case of  $\dot{m} = 7.49 \times 10^{-7}$  is depicted. The thick and thin black curves correspond to the same ones in figure 23. The red dashed and dash-dotted lines denote the primary curvature and inverse-Compton components, respectively. The blue dash-dot-dot-dotted line do the secondary emission via synchrotron and inverse-Compton processes outside the gap.

ponent (red dash-dotted line) cascades only to the secondary generation pairs, whose emission is represented by the blue dash-dot-dot-dotted line.

The curvature and IC luminosities are plotted as a function of  $\dot{m}$  in figure 25. It is clear that the IC process dominates the curvature one in the entire range of  $\dot{m}$  for super-massive BHs.

### 5.3.3. Cascaded pairs outside gap

The created pair densities between  $r_2$  and  $60 r_g$  are depicted as a function of  $\dot{m}$  in figure 26. In the same way as stellar-mass BHs (§ 5.1) and intermediate-mass BHs (§5.2), the magnetosphere becomes force-free outside the gap, as long as the gap solution exists.

Figures 17, 20 and 26 show that the BH magnetosphere becomes force-free for  $M = 10 M_\odot$ ,  $10^3 M_\odot$ ,  $10^5 M_\odot$ , and  $10^9 M_\odot$ . Indeed, a BH magnetosphere becomes force-free irrespective of the BH mass, as long as a stationary gap is sustained in it by  $\dot{m} > \dot{m}_{\text{low}}(M)$ .

### 5.3.4. Dependence on RIAF soft photon field density

Let us quickly examine how the gap luminosity depends on the ADAF photon field density, fixing  $\dot{m}$  so that

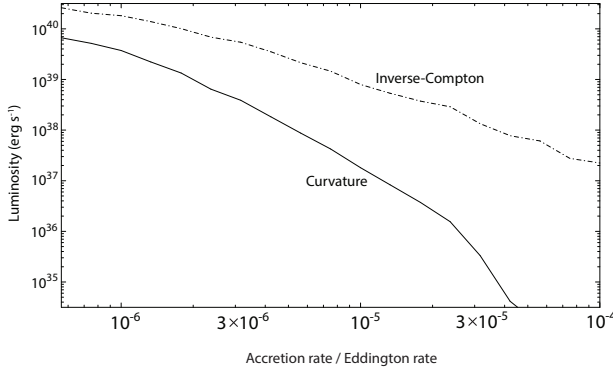


FIG. 25.— Gap luminosity as a function of the dimensionless accretion rate for a super-massive black hole with  $M = 10^9 M_\odot$  and  $a_* = 0.9$ . The solid and dash-dotted curves denote the luminosity of the curvature and inverse-Compton processes, respectively.

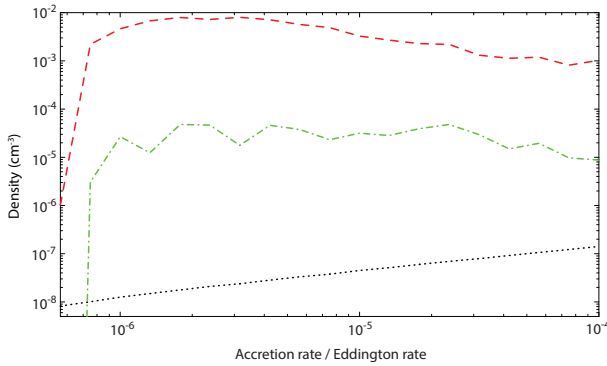


FIG. 26.— Similar figure as figure 17, but for a super-massive BH case,  $M = 10^9 M_\odot$ . The dashed and dash-dotted curves denote the densities,  $N_\pm$ , of the secondary and tertiary pairs, while the dotted one the GJ value,  $N_{GJ}$ .

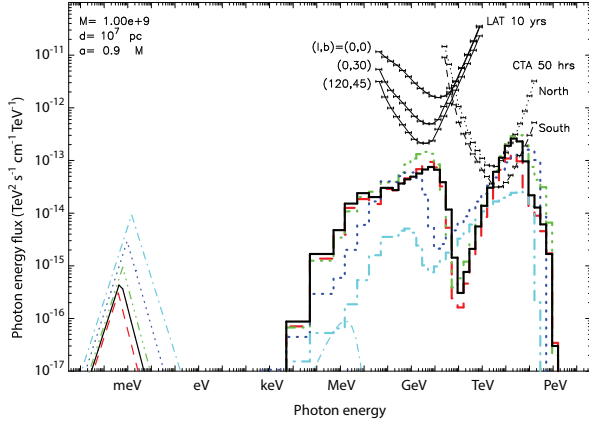


FIG. 27.— Similar figure as figure 23, but the ADAF photon field is artificially reduced to one-fourth by adopting  $R_{\min} = 12r_g$ , instead of  $R_{\min} = 6r_g$ .

the magnetic field near the horizon may not be changed. As a test model, we artificially reduce the photon density near the horizon to one-fourth of its original value by doubling  $R_{\min}$ . In figure 27, we plot the gap spectra for  $R_{\min} = 12r_g$ . We find that the gap emission increases because of the diminished soft photon density, as expected. To predict the gap spectrum of SMBHs further precisely, we must constrain the specific intensity of the RIAF photon field near the horizon such as by numerical simulations.

#### 5.4. Gap luminosity for various BH masses

Finally, we apply the method to various BH masses from  $10M_\odot$  to  $6.4 \times 10^9 M_\odot$ . The filled circles in figure 1 denote the solved  $\dot{m}_{\text{low}}(M)$  for  $(a_*, \Omega_F/\omega_H, R_{\min}/r_g) = (0.9, 0.5, 6)$ . It follows that  $\dot{m}_{\text{low}}(M)$  always lies below the upper limit,  $\dot{m}_{\text{up}}$  (upper straight line). Therefore, BH gaps exist for arbitrary BH masses.

We fit the filled circles in figure 1 with a straight line by least square method to obtain  $\lg \dot{m}_{\text{low}} = -3.6 - 0.26 \lg(M/M_\odot)$ . The luminosity,  $L_{\text{gap}}$ , of a BH gap, could be estimated by substituting this  $\dot{m} \approx \dot{m}_{\text{low}}$  into  $L_{\text{gap}} \approx 0.3L_{\text{BZ}} \approx 1.5 \times 10^{38} \dot{m} M_1 \text{ ergs s}^{-1}$ , where equation (3) is used. The factor 0.3 comes from the fact that the gap luminosity can attain at most  $\sim 30\%$  of  $L_{\text{BZ}}$ , because  $E_\parallel$  is partly screened by the created pairs within the gap, and because a stationary gap solution can possess only a sub-GJ current density. It is also noteworthy that the BH-gap solution at such a low  $\dot{m}$  corresponds to the case of the middle-aged pulsars whose outer-gap luminosity attains at most  $30\%$  of the spin-down luminosity from the same reasons (Hirotani 2013).

If we artificially change  $R_{\min}$ , we can consider the impact of the ADAF photon field density, without changing  $B$  at the same  $\dot{m}$ . In figure 1, we plot the  $\dot{m}_{\text{cr}}(M)$  for  $(a_*, \Omega_F/\omega_H, R_{\min}/r_g) = (0.9, 0.5, 12)$  as the open squares. It follows that the reduction of the soft photon field (by doubling  $R_{\min}$ ) changes the gap solution to some extent, because it affects the pair production process in the gap.

In figure 1 we also plot a slower BH spin,  $(a_*, \Omega_F/\omega_H, R_{\min}/r_g) = (0.5, 0.5, 6)$  as the open circles. It follows that  $\dot{m}_{\text{low}}(M)$  has a weak dependence on  $a_*$  due to the negative feedback effect (Hirotani 2013). To further constrain  $\dot{m}_{\text{low}}(M)$ , we need to specify the specific intensity of the RIAF (e.g., ADAF) photon field near the horizon by numerical computation. Such details are, however, out of scope of the present paper. Therefore, the region  $\dot{m} < \dot{m}(M)$  (in which stationary gaps do not exist) is depicted in red *gradation* in figure 1.

## 6. DISCUSSION

To sum up, we have solved stationary lepton accelerators (or gaps) in the magnetospheres of rotating black holes with arbitrary masses. By solving the set of an inhomogeneous part of the Maxwell equations, lepton equations of motion, and the radiative transfer equation, we demonstrate that an electric field arises along the magnetic field line around the null charge surface on which the frame-dragging angular frequency coincides with the magnetic-field angular frequency. In the gap, electrons and positrons are created via two-photon collisions and accelerated in opposite directions by the acceleration electric field into ultra-relativistic energies. Such leptons emit copious  $\gamma$ -rays via curvature and inverse-Compton (IC) processes, leading to a pair-production cascade inside and outside the gap. The gap longitudinal width is self-regulated so that a single electron eventually cascade into a single pair within the gap, and approximately coincides with the mean-free path (for an IC photon to materialize via two-photon collision) divided by the number of IC photons emitted by a single electron. As the accretion rate decreases, the increased mean-free path results in an extended gap, and hence an increased

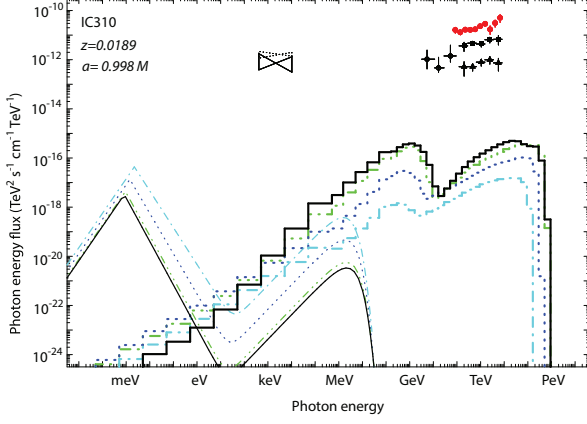


FIG. 28.— BH gap emission spectrum of IC310\*. Extreme spin,  $a_* = 0.998$ , is assumed to compare with figure 13 ( $B = B_{\text{eq}}$  case) of HP16. The cyan, blue, green, and black curves correspond to  $\dot{m} = 1.00 \times 10^{-5}$ ,  $3.16 \times 10^{-6}$ ,  $1.00 \times 10^{-6}$ , and  $7.49 \times 10^{-7}$ , respectively. The black triangles and squares show the observed fluxes in the low and high states (Aleksic et al. 2011) respectively, while the red circles show those in the flaring state (Aleksic et al. 2014b). The observed VHE fluxes are corrected for the absorption by the extragalactic background light. The solid bowtie represents the X-ray fluxes obtained by re-analyzing the observational data taken with *XMM-Newton* in 2003, *Chandra* in 2004, and *Swift* in 2007 (Aleksic et al. 2014a). The dotted bowtie represents the re-analyzed data of *Chandra* in 2005 (Aleksic et al. 2014a). The open circles denote the *Fermi*/LAT spectrum.

luminosity. The gap luminosity maximizes when the gap width becomes much greater than the horizon radius. For stellar-mass BHs, we can expect that their curvature emission are detectable with *Fermi*/LAT and the IC emission with *CTA*, when the BH binary is in a quiescent state, provided that the distance is within several kpc. For super-massive BHs, their IC emission may be marginally detectable with *CTA* for low luminosity AGN, if their distances are within a few tens of Mpc.

### 6.1. Improvement from HP16

In the present work, there are mainly two improvements from HP16, which formulated a BH gap model and applied it to the radio galaxy IC310. First, in the present work, the Poisson equation (15) is solved general-relativistically on the poloidal plane. However, in HP16, the left-hand side of equation (15) was approximated one-dimensionally in the Newtonian limit. Second, in the present work,  $\rho(r, \theta)$  (in the Poisson equation) is solved from the local pair production rate in a consistent manner with the radiative transfer equation. However, HP16 assumed that  $\rho(r)$  changes linearly with  $r$  (see their eq. 10).

Both above-mentioned simplifications suppress  $E_{\parallel}$  to some extent, comparing the GR treatment. To compare the difference, we apply the present 2-D, GR method to IC310, assuming  $B = B_{\text{eq}}$ . Figure 28 show the resultant SED, where the parameter set is basically the same as HP16; namely, we adopt  $a_* = 0.998$  and  $\Omega_F = 0.3\omega_H$ . Comparing with figure 13 of HP16, which was obtained for  $B = B_{\text{eq}}$ , we find that the 1-D Newtonian approximation in HP16 underestimated the gap luminosity about 1.5 times from the present 2-D GR treatment.

### 6.2. Rigidity of rotating magnetic field lines

We have assumed that  $\Omega_F \equiv F_{tr}/F_{r\varphi} = F_{t\theta}/F_{\theta\varphi}$  is constant along each magnetic field line. However,  $\Omega_F$

is not conserved when the electric potential drop along the magnetic field line becomes a non-negligible fraction of the electro-motive force exerted across the horizon. Nevertheless, for all the cases in the present paper, the gap luminosity is less than two percent of the Blandford-Znajek power. Noting that the particle energy is predominantly converted into radiation within the gap, we can conclude that the deviation of  $\Omega_F$  from a constant value (e.g.,  $0.5\omega_H$ ) is at most a few percent. Thus, the assumption of a constant  $\Omega_F$  along each magnetic field line is mostly justified.

### 6.3. Gap position versus the separation surface

It is worth comparing the gap position with the separation surface where both inflows and outflows start without  $E_{\parallel}$ . Since the plasma particles will not be accelerated either outward or inward at this surface, the sum of the gravitational, Lorentz and centrifugal forces will vanish along the magnetic field lines there. One of the convenient ways to find such a surface is to put both  $u_p = 0$  and  $u_p' = 0$  in the poloidal wind equation of MHD (Camenzind 1986a,b), where  $u_p$  refers to the poloidal velocity of the fluid. Note that this MHD argument is valid in the magnetically dominated limit, which is close to (but not equal to) the force-free limit.

In a stationary and axisymmetric BH magnetosphere, the separation surface is determined by the condition  $k_0' = 0$  in MHD (see end of § 3; Takahashi et al. 1990), where the prime denotes the derivative along the poloidal magnetic field line. For a radial poloidal field lines,  $k_0$  attains its maximum value 0.651, 0.478, 0.372, and 0.310 at  $r = 8.34r_g$ ,  $5.21r_g$ ,  $4.02r_g$ , and  $3.45r_g$ , along the field lines at  $\theta = 15^\circ$ ,  $30^\circ$ ,  $45^\circ$ , and  $60^\circ$ , respectively. Thus, the separation surface is approximately located at  $5r_g < r < 8r_g$  at  $\theta < 30^\circ$ .

As for the gap position, figures 3, 4, and 21 show that  $E_{\parallel}(r, \theta)$  distribution, and hence the gap longitudinal extent little depends on  $\theta$ , except near the meridional boundary,  $\theta \sim \theta_{\text{max}} = 60^\circ$ . Thus, near the magnetic pole (e.g.,  $|\theta| < 30^\circ$ ), the separation surface is generally located outside the gap (figs 8 & 22). This conclusion little depends on the poloidal magnetic field structure, because the gap solution is essentially determined by the  $\rho_{G,J}$  distribution, which is governed by the radial component of the magnetic field near the horizon (eq. 24) and because the separation surface distribution has a weak dependence on the poloidal field structure as well (fig. 2 of HP16).

If a plasma fluid begins to flow with  $u_p \approx 0$  from the separation surface, the plasma particles are accelerated up to the Lorentz factor of a few by the MHD interaction (e.g., eq. 5.2 of Hirokani et al. 1992). On the other hand, the electron-positron pairs that cascaded from outward-propagating PeV  $\gamma$ -rays have typical Lorentz factors  $\sim 10^6$  (for stellar-mass BHs). Thus, such pairs continue their outward motion across the separation surface, climbing up the ‘hill’ of the MHD effective potential  $k_0$  (fig. 2 of HP16) very easily. In another word, the large charge-to-mass ratio of the electron makes the electrostatic acceleration dominate the MHD acceleration, which is comparable to the centrifugal or gravitational one. Only in the direct vicinity of the horizon, the plasma mass and the causality at the horizon makes the gravitational interaction overcome the elec-

tromagnetic one. In another word, we can forget about the separation surface when we consider the formation of a gap in a BH magnetosphere.

It is worth noting that the above-mentioned MHD separation surface is distinct from what is argued in recent MHD simulations. In numerical simulations, the flow density decreases to zero at a specific surface, which requires an imposition of ‘density floors’. Without the density floors, a vacuum would develop in the funnel. However, such a limitation of numerical MHD has nothing to do with the gap formation discussed in the present paper.

#### 6.4. The case of very small accretion rate

Let us discuss what is expected when  $\dot{m}$  becomes even less than  $\dot{m}_{\text{low}}(M)$ . The ADAF photon field peaks around eV for stellar-mass BHs and around meV for super-massive BHs. These photons are emitted from the inner-most region,  $r \sim R_{\text{min}} \sim 6r_g$ , and decreases outward approximately by  $r^{-2}$  law. Thus, when the gap outer boundary is located at  $r \gg R_{\text{min}}$ , as in the case of  $\dot{m} \sim \dot{m}_{\text{low}}(R)$ , stationary pair production can be sustained only marginally in an extended gap. However, at  $\dot{m} < \dot{m}_{\text{low}}(R)$ , a stationary pair production can be no longer sustained and a vacuum region develops in the entire polar funnel. In this vacuum region, migratory leptons are accelerated by the vacuum  $E_{\parallel}$  and cascade into copious primary electrons and positrons accelerated in opposite directions. Emissions from such cascading primaries will be time-dependent and may consist of many ‘shots’, whose power spectrum density (PSD) may show some characteristic power law. In this case, the lower cutoff frequency of the power-law PSD will be given by the reciprocal of the light crossing time of the extended gap, which is much longer than the horizon-light-crossing

time scale.

#### 6.5. Distinction between gap and jet emissions

We finally discuss how to discriminate the gap and jet emissions. It follows from figure 9 that the gap HE and VHE fluxes increases with decreasing  $\dot{m}$ . That is, we can predict an *anti-correlation* between the IR/optical and HE/VHE fluxes. It forms a contrast to the standard shock-in-jet scenario, in which the IR/optical and the HE/VHE fluxes will correlate. Therefore, we propose to simultaneously observe nearby black hole transients during quiescence both in near-IR/optical and VHE. If their time-varying multi-wavelength spectra show anti-correlation, it strongly suggests that the photons are emitted from the BH gap. For nearby low-luminosity AGNs, the anti-correlation will appear between submillimeter wavelength and VHE.

In X-rays, the gap emission is very weak. Thus, if X-ray photons are detected, they are probably emitted from the jet or from the accretion flow.

Stellar-mass BHs exhibit the strongest gap emission in HE. Figure 9 shows that nearby BH transients are capable of emitting an order of magnitude greater fluxes than the LAT detection limit (with 10 years observation). It means that a HE ‘flare’ could be detected by *LAT* if the flare lasts for a month or so, particularly for the sources located away from the galactic plane. We will examine the plausible sources in a subsequent paper.

One of the authors (K. H.) is indebted to Dr. T. Y. Saito for valuable discussion on the CTA sensitivity, and to Drs. K. Kashiyama, K. Asada, M. Nakamura, A. K. Harding, D. Kazanas, S. Shibata for fruitful discussion. This work is supported by the Theoretical Institute for Advanced Research in Astrophysics (TIARA) operated under Academia Sinica.

#### REFERENCES

- Aleksić, J. et al. 2010, ApJ723, L207  
 Aleksić, J. et al. 2014,  $\dot{a}$ 563, A91  
 Aleksić, J. et al. 2014, Science, 346, 1080  
 Beskin, V. S., Istomin, Ya. N., & Par’ev, V. I. 1992, Sov. Astron., 36(6), 642  
 Beskin, V. S., Zheltoukhov, A. A. 2013, Astron. Lett., 39, 215  
 Bisnovatyi-Kogan, G. S., Ruzmaikin, A. A. 1974, Ap&SS, 28, 45  
 Blandford, R. D., & Znajek, R. L. 1976, MNRAS, 179, 433  
 Bogovalov, S. V. 1999, A&A, 349, 1017  
 Boyer, R. H. & Lindquist, R. W. 1967 *J. Math. Phys.*, 265, 281  
 Broderick, A. E., Tchekhovskoy A. 2015, ApJ, 809, 97  
 Camenzind, M. A. 1986a, A&A, 156, 137  
 Camenzind, M. A. 1986b, A&A, 162, 32  
 Cheng, K. S., Ho, C. & Ruderman, M. 1986a, ApJ, 300, 500  
 Cheng, K. S., Ho, C. & Ruderman, M. 1986b, ApJ, 300, 522  
 Cheng, K. S., Ruderman, M. & Zhang, L. 2000, ApJ, 537, 964  
 Chiang, J. & Romani, R. W. 1992, ApJ, 400, 629  
 Daugherty, J. K. & Harding, A. K. 1982, ApJ, 252, 337  
 Dermer, C. D. & Sturmer, S. J. 1994, ApJ, 420, L75  
 Goldreich, P., Julian, W. H., 1969, ApJ, 157, 869  
 Ghosh, P., Pethick, C. J., Lamb, F. K. 1977, ApJ, 217, 578  
 Harding, A. K., Tademaru, E. & Esposito, L. S. 1978, ApJ, 225, 226  
 Hassan, T., Arrabito, L., Bernlöhr, K., Bregeon, J., Hinton, J., Jogler, T., Maier, G., Moralejo, A. et al. 2015, In Proc. of the 34th International Cosmic Ray Conference (ICRC2015), The Hague, The Netherlands. arXiv:1508.05894  
 Hawley, J. F., Krolik, J. H. 2006, ApJ, 641, 103  
 Hirose, S. Krolik, J., de Villiers, J.-P., Hawley, J. F. 2004, ApJ, 606, 1083  
 Hirotani, K. Takahashi, M., Nitta, S., Tomimatsu, A. 1992, ApJ, 386, 455  
 Hirotani, K. & Okamoto, I. 1998, ApJ, 497, 563  
 Hirotani, K., & Shibata, S. 1999, MNRAS, 308, 54  
 Hirotani, K., & Shibata, S. 1999, MNRAS, 308, 67  
 Hirotani, K. 2006, Mod. Phys. Lett. A (Brief Review), 21, 1319  
 Hirotani, K. 2013, ApJ, 766, 98  
 Hirotani, K. 2015, ApJ, 798, L40  
 Hirotani, K., Pu, H.-Y. 2016, ApJ, 818, 50  
 Holloway, N. J. 1973, Nature Phys. Sci., 246, 6  
 Ichimaru, S. 1979, ApJ, 214, 840  
 Kerr, R. P. 1963, Phys. Rev. Lett., 11, 237  
 Koide, S., Shibata, K., Kudoh, T., Meier, D. L., 2002, Science, 295, 1688  
 Krolik, J. H., Hawley, J. F., Hirose, S. 2005, ApJ, 622, 1008  
 Levinson, A., Rieger, F. 2011, ApJ, 730, 123  
 Mahadevan, R. 1997, ApJ, 477, 585  
 McKinney, J. C., Gammie C. F., 2004, ApJ, 611, 977  
 McKinney, J. C., 2006, MNRAS, 368, 1561  
 McKinney, J. C., Narayan, R., 2007a, MNRAS, 375, 513  
 McKinney, J. C., Narayan, R., 2007b, MNRAS, 375, 531  
 McKinney, J. C., Tchekhovskoy, A., Blandford, R. D., 2012, MNRAS, 423, 3083  
 Mestel L., 1971, Nature, 233, 149  
 Miller-Jones, J. C. A., Jonker, P. G., MacCarone, T. J., Nelemans, G., & Calvelo, D. E., 2011, ApJ739, L18  
 Narayan, R., Yi, I., 1994, ApJ, 428, L13  
 Narayan, R., Yi, I., 1995, ApJ, 452, 710  
 Narayan, R., Igumenshchev, I. V., Abramowicz, M. A. 2003, PASJ, 55, L69  
 Neronov, A., Aharonian, F. A. 2007, ApJ, 671, 85

- O' Riordan, M., Pe'er A., McKinney, J. C. 2016, ApJ, 819, 95  
Plotkin, R. M., Gallo, E., Jonker, P. G. 2013, ApJ, 773, 59  
Romani, R. 1996, ApJ, 470, 469  
Romani, R. & Watters, K. P. 2010, ApJ, 714, 810  
Rybicki, G. B. & Lightman, A. P. 1979, Radiative Processes in Astrophysics (New York: John Wiley & Sons)  
Takahashi, M., Nitta, S., Tatematsu, Y., Tomimatsu, A. 1990, ApJ, 363, 206  
Takata, J., Shibata, S., Hirotani, K., and Chang, H.-K. 2006, MNRAS, 366, 1310  
Timokhin, A. N., 2010, MNRAS, 408, 2092  
Timokhin, A. N., Arons, J., 2013, MNRAS, 429, 20  
Timokhin, A. N., Harding, A. K., 2015, ApJ, 810, 144  
Tchekhovskoy, A., Narayan, R., McKinney, J. C. 2010, ApJ, 711, 50  
Pètri, J. & Kirk, J. G. 2005, ApJ, 627, L37  
Pètri, J. 2013, MNRAS, 434, 2636  
Wang, Y., Takata, J. & Cheng, K. S. 2011, MNRAS, 414, 2664  
Zhang, J. L. & Cheng, K. S. 1997, ApJ, 487, 370